Streptococcal meningoencephalitis dynamically shapes developmental monocyte and macrophage trajectories in the CNS

Authors: Vitka Gres[1], Florens Lohrmann[1,2], Vidmantė Fuchs[3,4], Jana Neuber[1], Zohreh Mansoori Moghadam[1], Anne K. Lösslein[1,6], Lance F. P. Bosch[1,3,4], Tiago Figueiral-Martins[1,3,7], Sebastian Baasch[1,8], David Obwegs[3,12], Gianni Monaco[4,9,10], Julia Henschel[3,4], Klaus P. Knobeloch[4,5], Marco Prinz[4,5], Steffen Jung[11], Katrin Kierdorf[1,4,5], Sagar[12], Julia Kolter[1], Daniel Erny[4†], Philipp Henneke[1,5, 13*†]

Affiliations:

[1]Institute for Infection Control and Prevention, Medical Center and Faculty of Medicine, University of Freiburg; Freiburg, Germany.

[2]Department of Pediatrics and Adolescent Medicine, Medical Center and Faculty of Medicine, University of Freiburg; Freiburg, Germany.

[3]Faculty of Biology, University of Freiburg; Freiburg, Germany.

[4]Institute of Neuropathology, Faculty of Medicine, University of Freiburg; Freiburg, Germany.

[5]Centre for Integrative Biological Signalling Studies (CIBSS), University of Freiburg; Freiburg, Germany.

[6]Institute of Medical Microbiology and Hygiene, Medical Center and Faculty of Medicine, University of Freiburg; Freiburg, Germany.

[7]Spemann Graduate School of Biology and Medicine (SGBM), University of Freiburg; Freiburg, Germany.

[8]Freiburg Institute for Advanced Studies (FRIAS), University of Freiburg; Freiburg, Germany.

[9]Single-Cell Omics Platform Freiburg, Faculty of Medicine, University of Freiburg; Freiburg, Germany.

[10]Institute for Transfusion Medicine and Gene Therapy, Medical Center, University of Freiburg; Freiburg, Germany.

[11] Department of Immunology and Regenerative Biology, Weizmann Institute of Science; Rehovot, Israel.

[12] Department of Medicine II, University Medical Center, Medical Faculty, University of Freiburg; Freiburg, Germany.

[13] Centre for Chronic Immunodeficiency, University Medical Center, Medical Faculty, University of Freiburg; Freiburg, Germany.

[†]Equal contribution

[*]Correspondence: philipp.henneke@uniklinik-freiburg.de

Abstract: Macrophages in the meninges, especially in the dura mater sheathing the brain from the skull, are involved in the immune defense of the central nervous system (CNS). However, their site-specific origin and function, both in steady state and in bacterial CNS infections are

incompletely understood. Using an intravenous model of streptococcal meningoencephalitis that mimics hematogenous dissemination in humans, we found that bacteria accumulated predominantly in the leptomeninges and dura, whereas invasion into the brain parenchyma was rare. However, monocyte infiltration into the leptomeninges and parenchyma strongly correlated with disease severity.
In the dura, infection triggered activation and loss of resident macrophages, followed by rapid engraftment of inflammatory monocytes that transiently replenished the dural macrophage niche. Under homeostasis, dural monocytes were supplied independently of CCR2 from adjacent skull bone marrow. In infection, however, this local reservoir was rapidly exhausted, and the markedly increased demand for monocytes required mobilization from peripheral bone marrow sources, revealing context-dependent heterogeneity in monocyte origin. Infection also reshaped ontogeny of this differential monocyte output, with an increase in Monocyte-Dendritic Cell Progenitor - derived monocytes (MDP-Mo). MDP-Mo exhibited enhanced MHC-II expression and persisted in the brain during the resolution phase together with $CD4^+$ T cells, suggesting a role in antigen presentation after bacterial clearance.

Together, these findings reveal a highly dynamic and compartment-specific remodeling of monocyte ontogeny, recruitment, and differentiation across CNS borders during bacterial meningoencephalitis. These mechanisms may offer opportunities for therapeutic interventions in the future.

One Sentence Summary: Streptococcal meningoencephalitis disrupts homeostatic, skull bone marrow-derived monocyte and macrophage trajectories in the dura.

Main Text:

2. INTRODUCTION

Bacterial meningoencephalitis is a devastating disease that affects millions of people each year. Group B streptococcus (*Streptococcus agalactiae*, GBS) is a common colonizer of the gastrointestinal and urogenital tract, but also a leading cause of neonatal meningoencephalitis. GBS poses a particular risk to patients with diabetes mellitus, pregnant women, the elderly, and immunocompromised people (*1*). GBS meningoencephalitis has a mortality rate of up to 10%, and surviving patients often suffer from neurological sequelae (*2*, *3*).

The integrity of the brain is protected by anatomical barriers that ensure the controlled passage of molecules from the periphery into the central nervous system (CNS). The choroid plexus, the perivascular space along the vessels, and the meninges harbor populations of macrophages (Macs), together called CNS-associated macrophages (CAM). They play a crucial role in maintaining homeostasis of the CNS, but also provide neuroprotection in many pathologies (*4–7*). Anatomically, the meninges consist of three layers – *dura mater*, as well as *arachnoid* and *pia mater* (leptomeninges) (*8*). The dura harbors a complex immunologic landscape that includes T- and B-cells, natural killer cells, neutrophils, plasmacytoid dendritic cells (pDCs), conventional DCs (cDCs), mast cells, monocytes, and diverse subsets of the most abundant population – dural

macrophages (DM) (*9*).

Dural sinuses, which drain venous blood, are sites of antigen sampling and presentation (*10*). The dura is connected to the skull marrow by ossified channels, which provide a direct migration route for monocytes, neutrophils and B-cells (*11*, *12*). Recently, cerebrospinal fluid has been described to transport bacteria from the dura to the skull marrow when bacteria like *Streptococcus pneumoniae* were directly injected into the cisterna magna (*13*). However, the dynamics of the dura–skull marrow immune axis in blood-borne bacterial infection remain unclear.

In contrast to the dura, the brain parenchyma contains only one resident immune population in steady state – microglia (MG). In a healthy brain, MG are highly unlikely to encounter peripheral immune cells such as neutrophils, T cells or monocytes. In contrast, neuroinflammatory diseases, e.g., multiple sclerosis (*14*) or ischemic stroke (*15*) can lead to leakage of the blood-brain barrier and infiltration of peripheral leukocytes, contributing to MG activation and disease exacerbation.

During GBS infection in the CNS, neuroimmune communication appears to be crucial. On the one hand, MG are thought to exacerbate immunopathology in infection, e.g., by producing nitric oxide, which ultimately leads to neuronal death (*16*). On the other hand, nociceptors of the trigeminal ganglia in the dura dampen the response of DM through CGRP-RAMP1 signaling, which leads to increased spread of bacteria into the brain parenchyma (*17*). Hence, the cross-talk of the immune compartments in the CNS parenchyma and interfaces seem to play major roles in disease progression and outcome. However, a deeper understanding of the precise immune cell dynamics in the CNS and particularly its borders during streptococcal meningoencephalitis is still lacking.

Here, we investigated the discrete immune responses of MG, DM, and infiltrating monocytes in streptococcal meningoencephalitis caused by hematogenous spread. We took an integrated approach to understand the intersectionality of myeloid fates in infection, focusing on localization and differentiation trajectories. This allowed us to demonstrate that DM are positioned at the primary interface of the infection, initiating immune activation. Infiltrating Ly6C^{hi} monocytes actively replenished resident DM and were imprinted by their cellular origin. Moreover, monocyte invasion into the adjacent CNS parenchyma was associated with adverse infection outcome. Thus, streptococcal infection induces fundamental ontogenetic and functional changes in tissue-resident macrophages of the CNS interfaces, and the recruitment pathways and differentiation dynamics of migrating monocytes are linked to disease advancement.

3. RESULTS

3.1 Hematogenous GBS infection highlights the meninges as a reactive CNS barrier

Previous studies on the immune responses in bacterial meningoencephalitis in mice typically relied on disease models in which the pathogen was directly injected into the *cisterna magna* (*13*, *18*, *19*), therefore circumventing the effects of peripheral immune activation and systemic bacterial dissemination on CNS inflammation. In streptococcal meningoencephalitis, mucosal colonization usually precedes CNS infection, and bacterial dissemination via the blood is often observed (*20*). To investigate the systemic dissemination of GBS and its capacity to invade the

122 CNS, we intravenously injected wild type (*Wt*) mice with $5x10^7$ CFU of the serotype III
123 hypervirulent BM110 GBS strain, which is linked to neonatal meningoencephalitis in humans
124 (*21*, *22*). The infection spread rapidly and the overall fitness of the infected mice drastically
125 declined until 3 days post infection (dpi) when mice lost around 20% of their body weight,
126 leading to termination of the experiments (Fig. S1A). We therefore focused on 2 dpi timepoint, at
127 which we observed bacterial presence in blood, brain lysates including leptomeninges, dura
128 mater, liver, skull and femur (Fig 1A). In agreement with previous data on GBS sepsis (*23*),
129 interleukin (IL)-6 levels in the plasma (Fig. S1B) as well as tumor necrosis factor (TNF), IL-1β
130 and interferon (IFN)-β in the brain lysates of infected mice were substantially increased (Fig.
131 S1C).

132 Detailed spatial mapping revealed that GBS dissemination into the brain parenchyma was rare,
133 indicating that CNS border tissues effectively restricted bacterial entry (Fig. 1B, S1D). While
134 bacteria were present in the choroid plexus at low levels (Fig. 1C, D, S1E), they accumulated
135 predominantly at the leptomeninges and the dura mater (Fig. 1B, E, S1D, S1F). This containment
136 implied active immune responses, prompting us to next examine immune cell recruitment in
137 response to GBS invasion. Flow cytometry analysis showed a significant influx of $Ly6C^{hi}$
138 monocytes into the brain, including the leptomeninges, while neutrophil numbers were only
139 marginally increased (Fig.1F, S1G). Monocyte influx positively correlated with the bacterial
140 burden in the brain (including leptomeninges) ($r > 0.9$), and in the mice with severe infections,
141 monocyte counts increased more than 50-fold compared to less affected mice (Fig.1G). In contrast,
142 the dura of GBS infected mice showed an increase in both monocyte and neutrophil counts
143 (Fig.1H). Moreover, resident DM numbers in infection were significantly reduced, both within the
144 sinuses and in extra-sinus area (Fig.1I, J). While DM have been previously characterized as MHC-
145 II^{hi} or MHC-II^{low}, both subsets declined proportionally during infection, with unchanged subset
146 frequencies (Fig.S1H, I).

147 To spatially validate both GBS localization and bone marrow-derived myeloid cell influx, we
148 utilized $Ms4a3^{Cre};R26^{Tomato}$ mice, in which granulocyte-monocyte progenitors (GMP) and their
149 progeny (including monocytes and neutrophils) are labeled. Coronal head sections from infected
150 $Ms4a3^{Cre};R26^{Tomato}$ mice showed robust accumulation of $Tomato^+$ myeloid cells in both dura and
151 leptomeninges, co-localizing with GBS foci (Fig.1K, S1J).

152 Collectively, these data show a compartmentalized pattern of GBS dissemination drastically
153 affecting the immune cell composition of the meninges and the brain. Considering that tissue
154 resident macrophages are the first responders in infection, we sought to investigate the
155 transcriptional changes of CNS resident macrophage populations upon the bacterial challenge.
156 Specifically, we focused on two distinct myeloid populations: DM and MG. To selectively label
157 long-lived DM, we employed $Mrc1^{CreERT2};R26^{Tomato}$ mice with tamoxifen-induced labeling
158 performed eight weeks prior to infection (Fig.1L). This timeline enabled us on one hand to
159 distinguish resident DM from newly recruited monocyte-derived cells in the dura, while allowing
160 us to discriminate between MG and other CAM on the other (Fig.S1K, L).

161 Principal component analysis (PCA) of the bulk RNA seq showed distinct clustering of the isolated
162 populations. Whereas MG from control and infected mice clustered closely together, DM from
163 infected and uninfected mice showed a distinct gene expression profile (Fig 1M). In line with our
164 previous data on peripheral GBS infection (*24*) many of the upregulated differentially expressed

genes (DEG) in DM and MG after GBS infection were associated with type I IFN signaling and with the defense response to bacteria, e.g., *Oasl2, Irf7, Usp18, Fcgr4, Gbp2, Ifit1, Oas3, Isg15,* and *Ifi44,* implying the existence of a common type I IFN-driven response of tissue resident macrophages to GBS (Fig.1N). While both populations mounted a similar core transcriptional response, the overall magnitude of gene induction expressed as $\log_2$(fold change) was higher in DM compared to MG (Fig.1O).

In summary, a strong inflammatory response and reduction of DM, coupled with a monocyte and neutrophil influx establishes the dura as a highly primary reactive immune interface in response to GBS infection.

3.2 Loss of dural macrophages triggers compensatory monocyte differentiation

Previous reports have shown that neuroinflammatory conditions such as infection or stroke enable monocyte engraftment into both the parenchyma and in the meninges (*18*, *25–27*). We therefore asked whether the changes in resident DM and MG described above were accompanied by high infection-driven monocyte-to-macrophage differentiation. As a baseline, we first examined monocyte-macrophage turnover in homeostasis using the *Cxcr4*^{CreERT2}*;R26*^{Tomato} mouse model, in which tamoxifen (TAM) induction labels hematopoietic stem cell (HCS)-derived cells, for up to six months (*28*). In steady state, MG are established early in embryonic development and do not receive substantial input from peripheral monocytes (*29*, *30*) and thus remained unlabeled throughout the experiment. In contrast, DM showed a gradual replacement by circulating monocytes, reaching up to 24% after 8 weeks and 45% at 16 weeks (Fig. S2A). Next, we assessed whether the infection altered DM and MG differentiation dynamics and analyzed *Cxcr4*^{CreERT2}*;R26*^{Tomato} mice 2 dpi that were treated with TAM 8 weeks prior (Fig. 2A). We did not detect Tomato$^+$ MG in the brain parenchyma or an increased frequency of Tomato$^+$ DM in infection (Fig. 2B). In the dura, however, GBS infection induced a marked expansion of late-Mo/early-Mac cells co-expressing Ly6C and CD206 (Fig. 2C, D). These Macs were of HSC origin (Fig. 2E) and, unlike Ly6C$^+$ dural monocytes, upregulated MHC-II (Fig. 2F). Therefore, this population likely represented a transient monocyte-to-Mac differentiation stage that facilitates repopulation of the DM compartment during infection, compensating for infection-driven DM loss.

To further explore changes of myeloid populations in depth, we performed single-cell transcriptional analysis on FACS sorted CD45$^+$CD11b$^+$ myeloid cells from control and GBS infected dura (Fig. 2G). Using unbiased hierarchical clustering analysis, we were able to distinguish 12 distinct cell clusters (Fig. 2H, S2B). Within the Mac compartment, all DM clusters expressed canonical DM genes, including *Mrc1*, *Pf4*, *Cd68*, and *Cx3cr1*, but each exhibited some distinct transcriptional features (Fig. S2B). Cluster 0 was enriched for type I IFN–responsive genes such as *Oasl1* and *Cxcl10*. Cluster 2 showed elevated expression of MHC-II–associated genes, consistent with enhanced antigen-presenting potential. Cluster 3 was marked by higher *Cbr2* expression, while cluster 4 was characterized by increased *Lyve1* (Fig. S2C). Furthermore, we identified three monocyte populations: classical monocytes, patrolling monocytes characterized by higher *Itgal* expression, and a distinct population that emerged specifically during infection and was virtually absent under homeostatic conditions (cluster 5) (Fig. 5H, S2B). We therefore refer

to this population as infection-associated monocytes, which exhibited elevated expression of antimicrobial and inflammatory genes, including *Nos2, Rsad2, Mif, Cfb, Cxcl9,* and *Ccl5,* compared to the other monocyte clusters (Fig. S2D).

Consistent with previous observations, a relative decrease of percentage in macrophage clusters (0,2,3,4, Fig. 2I) and an increase of percentage in neutrophil (1) and monocyte (5,6,7) clusters (Fig. 2J) corelated to the bacterial burden in the brain (Fig. S2E). DM, particularly clusters 0 and 3, upregulated necroptosis regulators *Mlkl, Ripk1* and *Zbp1*, indicating that their loss may involve necroptotic death pathways reported in other bacterial infections (Fig. S2F)(*31*, *32*). Conversely, the expression of *Mrc1*, *H2-Ab1* and *Cd74* in monocyte cluster 5 increased proportionally to the bacterial burden (Fig. 2K), consistent with accelerated monocyte-to-macrophage differentiation in response to infection-driven macrophage depletion (Fig. 2C–F).

Next, to functionally validate the rapid monocyte-to-macrophage differentiation observed during infection, we adoptively transferred monocyte progenitors (MP) isolated from *β-actin-GFP* mice into either infected or control mice (Fig. 2L, S2G). In infected mice, we detected robust engraftment of GFP^+ donor cells in the dura, with preferential accumulation in sinus-associated regions (Fig. S2H). A subset of these cells upregulated CD206 and acquired an ameboid morphology, consistent with acquisition of macrophage-like features (Fig. 2M, N). Overall, infection triggered a broad diversification of monocyte states and accelerated their differentiation into Macs, highlighting a remarkable degree of lineage plasticity within the inflamed dura.

3.3 Distinct monocyte sources support dural immunity in steady state and infection

Having established that infection induces extensive monocyte recruitment into the dura and the brain, we next wanted to determine their functional role in streptococcal infection. Since CCR2 is considered a key driver of monocyte mobilization from the bone marrow, we performed GBS infection in *Ccr2*$^{-/-}$ mice.

At 2 dpi, bacterial loads were similar between GBS-infected *Wt* and *Ccr2*$^{-/-}$ mice in the periphery and the brain, including leptomeninges (Fig. S3A), indicating that infiltrating $Ly6C^{hi}$ monocytes neither play a critical role in early bacterial control, nor were directly involved in bacterial dissemination into the CNS. Notably, steady state monocyte numbers in the dura were similar between *Ccr2*$^{-/-}$ and *Wt* mice (Fig. 3A), consistent with the observation that dural monocytes express significantly lower levels of *Ccr2* than circulating monocytes (Fig. S3B). In contrast, we did not observe a significant monocyte influx in *Ccr2*$^{-/-}$ mice in the dura or in the brain upon infection, compared to the situation in *Wt* mice (Fig. 3A, 3B). Lack of monocytes was not compensated for by higher numbers of infiltrating granulocytes during GBS infection, as *Ccr2*$^{-/-}$ mice showed even lower dural neutrophil numbers than *Wt* mice (Fig. S3C).

These findings indicate that, unlike classical inflammatory monocyte trafficking, homeostatic monocyte access to the dura occurs largely through a CCR2-independent mechanism, whereas CCR2 becomes critical during infection-induced monocyte mobilization. The persistence of monocytes in the dura of *Ccr2*$^{-/-}$ mice consequently raised the question of their anatomical origin.

246 Previous reports have highlighted the skull marrow as a primary source for monocytes and B-cells
247 replenishing the dura in homeostasis (*12*, *33*). In order to revisit this finding and evaluate the
248 contribution of the adjacent skull marrow during GBS infection, we transplanted bone marrow
249 from either *Cx3cr1*$^{+/gfp}$ or *β-Actin-GFP* mice, and in both cases, monocytes and monocyte-derived
250 DM coming from the donor were GFP-labeled. Recipient mice were subjected to either full body
251 irradiation or head-shielded irradiation, enabling us to discriminate between local (skull) versus
252 peripheral (femur) bone marrow contribution to the dural monocyte pool (Fig. 3C). In fully
253 irradiated mice, Ly6C^{hi} monocyte populations reached close to 100% chimerism after 8 weeks post
254 transplantation in all assessed compartments (Fig. 3D, S3D). In contrast, femurs of head-shielded
255 mice showed an incomplete chimerism as previously reported (*34*), while the skull marrow, which
256 was predominantly protected by head-shielding, had significantly less contribution of donor-
257 derived cells (Fig. 3D, S3D).

258 To understand donor-cell integration dynamics in dura and the bone marrow sites, we calculated
259 relative chimerism rates by comparing the ratios of GFP-positive monocytes from dura to skull
260 bone marrow or femur bone marrow (Fig. 3E). In fully irradiated mice, there was no difference in
261 monocyte populations at the three sites (Fig. 3F, S3E, S3F). In head-shielded mice, relative
262 chimerism showed that the dural monocytes closely mirrored the skull marrow chimerism (Fig.
263 3F). In contrast, femur monocytes had almost two times higher engraftment compared to dural
264 monocytes (Fig. 3F). Considering the relatively short lifespan of Ly6C^{hi} monocytes (*35*), these
265 results strongly suggested that, in steady state, the skull marrow dominated over peripheral bone
266 marrow as monocyte reservoir for the dura. Moreover, whereas more than 75% of DM were
267 replaced by donor-derived cells following full body irradiation, we found only 5% donor-derived
268 DM 8 weeks post irradiation with head-shielding (Fig. 3G). For comparison, fate-mapping
269 experiments indicate that ~24% of DM are normally replaced by monocytes over this timeframe
270 (Fig. S2A), suggesting that DM replacement is largely supported by skull-derived monocytes in
271 this setting.

272 To determine whether the skull bone marrow supply of monocytes persists during infection, we
273 infected head shielded chimeras 8 weeks after bone marrow transplantation with GBS (Fig. 3H).
274 The chimerism of the skull and femur monocytes were similar in infected and non-infected mice
275 (Fig 3K, S3H). In contrast, the percentage of donor-derived Ly6C^{hi} monocytes in the dura
276 significantly increased upon infection, indicating an accelerated recruitment from other (non-skull)
277 bone marrow sources (Fig. 3I, 3J, 3K, S3H, S3I). While monocytes were not detectable in the
278 control brain, infiltrating monocytes showed a comparable chimerism to monocytes in the dura
279 and femur upon infection in head-shielded mice, suggesting the peripheral influx in both
280 compartments (Fig. S3H). Therefore, the accelerated replacement dynamics under infection
281 indicated an extensive recruitment of monocytes from peripheral sources, without a preferential
282 anatomical bone marrow niche (Fig. 3I). Additionally, the acceleration of DM replacement by
283 donor-derived monocyte progenitors pointed to a faster monocyte-to-Mac differentiation in the
284 acute infection (Fig. 3L). Together, these results suggest that the previously proposed CCR2-
285 independent homeostatic replenishment of dura monocytes from the skull marrow does not suffice
286 to meet the highly increased demand for monocytes in streptococcal meningoencephalitis. In
287 addition and as reported before (*34*), irradiation let to a minor engraftment of donor-derived cells
288 to the brain MG pool, which was highly reduced in head shielded chimera (Fig. S3G, S3J). Donor-
289 derived cells in the infected head-shielded chimeras were mostly localized in the leptomeninges
290 and were not observed integrating into the MG pool (Fig. S3J).

Given these dynamic shifts in monocyte sourcing, we next investigated whether GBS infection alters myelopoiesis within the skull and femoral bone marrow compartments. Previous studies have demonstrated that bacterial infections can skew haematopoiesis toward emergency myelopoiesis (*36*). In our model, GBS was detected in both skull and femur bone marrow, suggesting direct bacterial engagement with hematopoietic niches (Fig. 3M, S3K). While the numbers of common myeloid progenitors (CMP) remained unchanged between control and infected mice (Fig. 3N), granulocyte-monocyte progenitors (GMP) were significantly depleted in both bone marrow compartments during infection (Fig. 3O, S4A). Furthermore, monocyte progenitors and monocyte-dendritic progenitors (MDP) were significantly reduced in the skull bone marrow, whereas they were only slightly reduced in the femur (Fig. 3P, Q, S4B). Despite these changes at the progenitor level, monocyte numbers in both skull and femoral bone marrow remained unchanged during infection (Fig. 3R).

These findings indicate that GBS infection imposes distinct pressures on myeloid populations within different bone marrow reservoirs. While both sites participate in emergency myelopoiesis, the skull marrow appears particularly vulnerable to progenitor depletion, potentially reflecting its rapid mobilization of monocytes to the connected dura.

3.4 GBS infection reprograms monocyte ontogeny toward MDP-derived lineages

Having observed a site-specific depletion of myeloid progenitor subsets prompted us to investigate whether GBS infection alters the ontogeny of monocytes originating from these sites. Under steady-state conditions, most monocytes arise from GMP derived from CMP, although a smaller subset can develop from MDP (*37–39*)(Fig. 4A). To distinguish between these developmental pathways, we utilized *Ms4a3*^{Cre}*;R26*^{Tomato} reporter mice, in which GMP-derived monocytes (GMP-Mo) and neutrophils are irreversibly labeled (*38*), whereas MDP-derived monocytes (MDP-Mo) remain Tomato-negative. During GBS infection, MDP-Mo frequencies increased in both skull and femur bone marrow (Fig. 5B), however, this shift was significantly more pronounced in the skull, consistent with the site-specific progenitor depletion due to emergency myelopoiesis, as described above (Fig. 3O-R). Importantly, neutrophils (Fig. S5A) and GMP-derived monocyte progenitors, such as common monocyte progenitor (cMoP), remained labeled in both skulls and femurs during homeostasis and infection, confirming that altered Tomato labeling reflected genuine changes in monocyte ontogeny rather than infection-induced recombination artifacts (Fig. S5C). On the other hand, MDPs remained Tomato-negative (Fig. S5B, S5F). Furthermore, to independently verify monocyte labeling, we used *Cxcr4*^{CreERT2}*;R26*^{Tomato} mice, in which TAM induction labels all HSC-derived cells (*28*) (Fig. 4A). Indeed, there was no difference in Tomato-labeling of monocytes in skull, femur or dura in infection (Fig. S5D, E).

Next, we analyzed if this ontogenic skewing was also evident in the dura during infection. Indeed, dural monocytes showed a marked increase in Tomato-negative MDP-Mo in *Ms4a3*^{Cre}*;R26*^{Tomato} mice (Fig. 4C). Of note, these MDP-Mo expressed CX3CR1 and displayed higher MHC-II levels compared to GMP-Mo (Fig. 4D, E).

330 To further delineate differences of MDP-Mo and GMP-Mo in the infected dura, we performed
331 single cell RNA sequencing. Monocytes were gated as $Lin^{neg}CD45^{+}CD11b^{+}Ly6C^{hi}CX3CR1^{+}$,
332 with Tomato used to distinguish between lineage origins (Fig. S5G). UMAP embedding did not
333 separate the two lineages into discrete clusters, indicating substantial transcriptional convergence
334 in the inflamed dural environment (Fig. 4F). Nonetheless, pseudo-bulk differential expression
335 analysis revealed clear lineage-associated signatures, including higher MHC-II gene expression in
336 MDP-Mo, consistent with flow cytometry (Fig. 4G). In total, 308 genes were differentially
337 expressed in MDP-Mo and 290 in GMP-Mo (Fig. 4H).

338 Comparison with a DEGs from published dataset of bulk RNA-seq from steady-state bone
339 marrow–derived MDP-Mo and GMP-Mo (GSE262369) (*39*) revealed partial overlap in signature
340 (Fig. 4I, 4J, S5H, I, J).

341 We then focused on DEGs that did not overlap with the steady-state dataset, reasoning that these
342 might represent infection-associated transcriptional programs. Gene ontology analysis showed that
343 GMP-Mo upregulated pathways related to mitochondrial respiration, oxidative phosphorylation,
344 and antimicrobial defense, consistent with an energetically demanding inflammatory response
345 (Fig. 4K). In contrast, MDP-Mo upregulated GO categories linked to immune system processes,
346 cell differentiation, response to external stimuli, and positive regulation of IL-17 production (Fig.
347 4L).

348 Together, these findings indicate that GBS infection not only alters the quantity of monocytes
349 recruited to the dura but also reshapes their developmental origins and transcriptional states, with
350 skull bone marrow producing disproportionately more MDP-Mo under inflammatory pressure.
351 This ontogenic reprogramming likely reflects differential stress imposed on bone marrow niches
352 and may contribute to functional diversification of monocyte responses at the CNS interfaces
353 during bacterial meningitis.

354

355 **3.5 Post-infection monocyte ontogeny diverges between dura and brain**

356 The infection-induced reprogramming of monocyte ontogeny, together with the high turnover of
357 dural macrophages, raised the question of how the CNS myeloid landscape is restored once
358 bacterial infection is resolved. Given that MDP-Mo expanded disproportionately during acute
359 GBS infection in dura compared to the steady-state, we hypothesized that monocyte dynamics and
360 their contribution to tissue macrophage pools might substantially change during the recovery
361 phase. GBS meningitis is fatal in mice without treatment, mirroring the clinical situation in
362 neonates. To model successful therapeutic intervention, we treated infected mice with ampicillin
363 and azithromycin for two weeks, beginning at 2 dpi (Fig. 5A). Bacteria became undetectable in
364 blood, brain and liver already at 7 dpi, confirming complete resolution of infection.

365 By 7 dpi, monocyte and neutrophil numbers in the dura were only modestly elevated and had fully
366 returned to baseline by 30 dpi (Fig. 5B, C). In contrast, dural macrophages expanded significantly
367 between 2 and 7 dpi (Fig. 5D), indicating a regenerative wave of macrophage replenishment during
368 recovery. In the brain, monocytes and neutrophils normalized by 7 dpi (Fig. 5E, 5F), although at

369 that timepoint, monocytes persisted at low levels in the leptomeninges and parenchyma (Fig. 5E,
370 K), suggesting ongoing immune activity beyond bacterial clearance.

371 Strikingly, lineage analysis revealed divergent kinetics of MDP-derived monocytes in the dura
372 versus the brain. In the dura, MDP-Mo peaked at 2 dpi and rapidly declined to homeostatic levels
373 during clearance (Fig. 5G, H). In contrast, brain MDP-Mo accumulated progressively and peaked
374 at 7 dpi, constituting over 40% of the monocyte pool at this time (Fig. 5I, J). Because MDP-Mo
375 expressed higher MHC-II than GMP-Mo and were enriched for GO terms associated with
376 lymphocyte activation and IL-17 production, we hypothesized that their delayed accumulation in
377 the brain may reflect a role in antigen presentation and T-cell activation. Indeed, $CD45^{+}CD11b^{neg}$
378 lymphocytes increased specifically in the brain (Fig. S6A), but not the dura (Fig. S6B), at 7 dpi.
379 Histological analysis of brain 7 dpi showed accumulation of $CD4^{+}$ T-cells in proximity of MHC-
380 II^{+} cells, of which most are found in CNS-border areas such as the ventricles or the leptomeninges,
381 but were also present in the brain parenchyma (Fig. 5K, S6D). On the other hand, at 2 dpi,
382 accumulation of monocytes was found in leptomeninges with very rare $CD4^{+}$ T-cell incidence,
383 while at 30 dpi neither monocytes nor $CD4^{+}$ T-cells are present in the brain (Fig. S6C).

384 We next asked whether GMP-derived monocytes contribute to restoration of the DM niche.
385 $Tomato^{+}$ DM in *Ms4a3*^{Cre};*R26*^{Tomato} mice transiently increased in the dura at 7 dpi but were back
386 to steady state levels at 30 dpi, indicating they only contribute to the DM compartment transiently
387 (Fig. 5L, M). Since MDP-Mo and MDP-derived Macs cannot be fate-mapped with currently
388 available tools, we assessed long-term DM maintenance using *Cxcr4*^{CreERT2};*R26*^{Tomato}mice induced
389 one week before infection. $Tomato^{+}$ DM frequencies were indistinguishable between infected and
390 control mice at 30 dpi (Fig. 5N), demonstrating that the DM niche is ultimately restored by long-
391 lived tissue-resident macrophages rather than recruited monocyte progeny. Similarly, microglia
392 remained Tomato-negative, indicating that CNS parenchymal macrophages do not undergo
393 substantial monocyte-derived replacement during or after GBS infection (Fig. S6E).

394 Thus, while the dura and brain recruit distinct monocyte populations during infection and early
395 recovery, both compartments ultimately revert to a resident cell–dominated homeostasis.

396

397 4. DISCUSSION

398 Acute streptococcal meningoencephalitis warrants major prevention efforts worldwide, due to its
399 substantial consequences for cognition and motor function in surviving patients (*40*). The
400 uniqueness of the disease in an individual's life is reflected by the long-standing concept of a
401 largely immune-privileged brain, which - unlike other internal organs, such as the liver and
402 kidneys, does not come into incidental contact with pathogens and peripheral immune cells (*41*).
403 Accordingly, most mechanistic insights have focused on MG, the resident immune cells of the
404 CNS, largely because of the assumption that they are the primary mediators of immune defense
405 within the CNS interior (*16*, *18*, *42*, *43*).

406 In contrast, very little information is available on the role of CAM in this context, despite the fact
407 that clinically, CNS borders play a central role in disease manifestation. This discrepancy is
408 probably due to the fact that until recently it was not possible to reliably distinguish between CAM

409 and parenchymal MG, and owed to the paucity of robust rodent meningitis models in which
410 bacteria are not injected directly into the CNS.

411 Lately, there has been increasing evidence that macrophages residing in brain barriers, particularly
412 in the meninges, play an important role in various neuropathologies (*4*, *5*, *44*). In addition, the
413 recent discovery of direct communication between the dura mater and skull bone marrow raises
414 the question of the role of distinct bone marrow sites in disease (*11–13*, *45*, *46*).

415 Accordingly, we have combined the latest tools in myeloid cell fate-mapping and
416 multidimensional analysis with a mouse model in which streptococci circulate systemically before
417 entering the CNS, as in a natural disease. In this model, we demonstrate that bacteria accumulate
418 primarily in the leptomeninges and dura, with minimal penetration into the brain parenchyma,
419 which aligns with emerging evidence that the meninges behave as a highly responsive
420 immunological interface (*47*, *48*).

421 Unlike perivascular and leptomeningeal macrophages, DM are replenished to a higher percentage
422 by monocytes in steady state, reaching around 45% DM replacement after 4 months. These
423 dynamics changed rapidly during the infection, characterized by the disappearance of resident DM
424 and a faster differentiation of incoming monocytes into a Ly6C^{+}CD206^{+}MHC-II^{+} macrophage
425 population, which is not discernible in steady state. scRNA-seq data from infected mice confirmed
426 the emergence of infection-associated monocytes which upregulated *Mrc1* and MHC-II genes
427 proportionally to the bacterial burden found in the brain. Additionally, adoptive transfer of
428 monocyte progenitors validated the capacity of monocytes to rapidly assume macrophage features
429 in the infected dura.

430 On the other hand, bacterial burden positively correlated to the loss of different DM clusters. It is
431 conceivable that these resident DM populations are the first responders in the early phase of
432 infection, leading to cellular stress and ultimately, cell death. This observation is consistent with
433 the so-called "macrophage disappearance reaction" which has been described in inflammation of
434 the peritoneal cavity (*49*, *50*), the liver (*31*) and other tissues (*51*) and which might serve to initiate
435 infection control. Infection-induced cell death of resident Macs has also been found in the
436 meninges in viral infection (*4*), accompanied by the engraftment of monocytes. Consistent with
437 this, the upregulation of canonical necroptosis genes *Mlkl, Ripk1* and *Zbp1* in DM clusters in
438 infection points to a likely mechanism of DM loss in our model.

439 The skull bone marrow can serve as a reservoir for myeloid cells, which directly supplies the dura
440 with monocytes (*12*). This finding is particularly interesting considering the great demand for
441 monocytes in meningoencephalitis, not only for the induction of inflammation, but also to serve
442 as potential Mac precursors in a niche emptying due to Mac death.

443 By using head-shielded bone marrow chimeras, we confirm the recent finding that the skull
444 marrow supplies the adjacent dura with monocytes in steady state (*12*). Remarkably, head-shielded
445 mice had less than 8% of donor-originating DM, whereas our fate-mapping experiments revealed
446 that monocyte replacement would reach around 24% over 8-week period. These results point to
447 the skull marrow as the primary source of monocytes for DM renewal in homeostasis. However,
448 infection alters homeostatic pattern of monocyte egress and differentiation. In infected head-
449 shielded mice, chimerism rates were significantly higher in dura and brain, suggesting that skull

marrow could not adequately meet the high demand for monocytes in meningoencephalitis and that other sources of hematopoietic progenitor cells were required. This observed „recruitment threshold“ during infection was paralleled by changes in skull marrow composition, particularly in monocytes and monocyte precursors, including GMP-derived monocyte progenitors (MP) and MDP. Together with the observed presence of GBS in the skull marrow, this implies the initiation of emergency hematopoietic programs. Indeed, our data support this shift in myelopoiesis. While the homeostatic dura hosts classical and non-classical monocytes, we found that in infection monocyte numbers substantially expanded, with a significant influx of transcriptionally distinct infection-associated monocytes. Furthermore, we show that, while the steady state dura can be replenished by monocytes in CCR2-independent manner, CCR2 was required for the infection-associated monocyte influx into the dura. It seems noteworthy that we did not find evidence that these infection-associated monocytes contributed to bacterial trafficking, as *Ccr2*$^{-/-}$ mice did not have a difference in bacterial load compared to *Wt* animals. This is consistent with studies that have identified numerous genes in GBS which facilitate bacterial adhesion to the endothelium, thereby enabling transcytosis and potentially crossing of CNS barriers (*21*, *52*, *53*). Our lineage tracing using *Ms4a3*^{Cre} mice uncovered infection-driven changes in monocyte ontogeny. While GMP-derived monocytes dominate in steady state, infection induced a substantial increase in MDP-derived monocytes, especially in skull marrow and the dura. MDP-Mo displayed elevated MHC-II and transcriptional programs associated with lymphocyte activation, differentiation, and IL-17 pathways. Whereas GMP-Mo expressed metabolic and antimicrobial pathways consistent with classical inflammatory responses, MDP-Mo appeared positioned to modulate adaptive immunity. Indeed, after the clearance of the infection by using antibiotics, we found more than 40% of MDP-Mo in the brain and leptomeninges, as well as CD4+ T-cells. Nonetheless, neither MDP-Mo nor GMP-Mo contributed lastingly to the DM or MG pools during recovery. Indeed, our *Cxcr4*^{CreERT2} fate-mapping analysis indicates that surviving tissue-resident cells restored the DM niche in the long term.

Nevertheless, additional work is needed to understand whether changes in monocyte ontogeny modify disease progression and to determine the cues that govern the transition from GMP- to MDP-derived monocyte production. Furthermore, GBS meningoencephalitis predominantly affects neonates and young infants, whose barrier tissues and immune system undergo rapid changes and differ from adults. These developmental differences likely influence the magnitude, kinetics, and cellular composition of the meningeal immune response. Thus, our model in 6–12 week old mice may not fully reflect the unique vulnerabilities of the perinatal CNS relevant to neonatal GBS infection. Future studies applying this infection paradigm to neonatal or early postnatal mice will be important to determine how age-dependent differences in barrier integrity, macrophage maturation, and monocyte ontogeny shape the trajectory of meningeal infection.

In summary, we have integrated fate mapping, microscopy and transcriptomic analysis to highlight a multilayered immune architecture at the CNS border during streptococcal meningoencephalitis. These insights reshape our understanding of myeloid dynamics during bacterial CNS infection, suggesting that monocyte origin, differentiation trajectory, and anatomical context collectively determine their function in disease. Furthermore, the vulnerability of skull marrow progenitors to bacterial invasion and depletion suggests that local hematopoietic niches may influence susceptibility or recovery potential in CNS infections.

494

495 **5. MATERIALS AND METHODS**

496 **1. Study design**

497 This study aimed to decipher changes in the myeloid populations in the CNS during
498 streptococcal meningoencephalitis, specifically focusing of microglia, dural macrophages
499 and monocytes. For that purpose, we used a combination of different fate mapping mouse
500 models, as well as microscopy, flow cytometry and transcriptomic analysis. Group sizes
501 and number of repetitions are indicated in the figure legends.

502 **2. Mice**

503 Both female and male mice from C57BL/6 genetic background were used at 6 to 12 weeks
504 of age. C57BL/6J and C57BL/6N mice were purchased from Jackson Laboratories (USA)
505 or Charles River Laboratories (Germany) and bred in the local animal facility. CD45.1-
506 mice (B6.SJL-Ptprca Pepcb/BoyJ) were purchased from Jackson Laboratories. *Cx3cr1*$^{gfp/+}$
507 mice were obtained as a kind gift from Steffen Jung (Weizmann Institute, Israel). *β-Actin*
508 *gfp+/− (C57BL/6-Tg(CAG-EGFP)131Osb/LeySopJ)* and *Ms4a3*^{Cre} (C57BL/6J-
509 Ms4a3em2(cre)Fgnx/J) mice were purchased from Jackson Laboratories. *Mrc1*^{CreERT2} mice
510 were provided by Marco Prinz (Institute of Neuropathology, Freiburg) as a kind gift.
511 *Cxcr4*^{CreERT2} mice were provided by Ralf Stumm (Neuropharmacology, Jena) as a kind gift.
512 *Ccr2*$^{-/-}$ (B6.129S4-Ccr2tm1Ifc/J) mice were bought from Jackson Laboratories (USA).
513 Mice were bred in animal facilities of the University of Freiburg under specific pathogen-
514 free conditions and were kept in groups of a maximum of five animals per cage at defined
515 environmental conditions. Food and water were available *ad libitum*, and day/night cycles
516 were set to 12 h. All animal experiments were approved by the Federal Ministry for Nature,
517 Environment and Consumer's protection of the state of Baden-Wuerttemberg (proposal
518 numbers G-19/031 and G23/008).

519

520 **3. Mouse interventions**

521 Induction of Cre recombinase by tamoxifen has been explained previously(*30*). Briefly,
522 mice were anesthetized by isoflurane inhalation. 4mg TAM in 200µl corn oil (both Sigma)
523 was injected subcutaneously in *Cxcr4*^{CreERT2} or *Mrc1*^{CreERT2} mice at two time points 48h
524 apart. As control, littermates with respective floxed alleles, but without Cre recombinase
525 expression, were treated in the same fashion.
526 For bone marrow transplantations, recipient mice were anesthetized using ketamine (100
527 mg/kg body weight) and xylazine (10 mg/kg body weight) administered intraperitoneally.
528 Mice were then head-shielded with a 6 mm lead plate, or not shielded and lethally irradiated
529 with 9 Gy. Subsequently, mice received $5x10^6$ donor-derived bone marrow cells
530 intravenously. Mice were analyzed 8 weeks post transplantation.
531 Mice treated with antibiotics were injected i.p. with ampicillin (100 µg/g body weight) and
532 azithromycin (50 µg/g body weight) dissolved in 100 µl sterile water at 2dpi, after which
533 they continued to receive antibiotics via the drinking water for up to two weeks (0.4 g/L

534 ampicillin and 0.2 g/L azithromycin). Control mice were injected with PBS, then treated
535 with antibiotics. Mice were analyzed either at 7 dpi or 30 dpi.
536
537 **4. GBS culturing and infection**
538 Prior to infection, GBS strain BM110 was streaked on a blood agar plate (Columbia agar
539 + 5% sheep blood; BioMérieux) and incubated at 37°C overnight. One colony from the
540 blood agar plate was transferred into 5 ml of Todd-Hewitt broth and incubated at 37°C
541 overnight. The overnight culture was inoculated into 200 ml warm Todd-Hewitt broth.
542 Bacteria were grown to the mid-log phase, and bacterial concentration was determined with
543 an optical spectrophotometer (OD600 = 0.4) and confirmed by serial dilutions plating onto
544 a blood agar plate. Afterwards, bacteria were washed twice with PBS and resuspended in
545 PBS at 10^9 CFU/ml. A total of 50 µl (5 x 10^7 CFU) suspension of bacteria or vehicle (PBS)
546 was injected into the retro-orbital venous plexus. For this procedure, mice were
547 anesthetized by isoflurane inhalation.
548
549 **5. CFU assay**
550 Mice were sacrificed by CO_2 inhalation after which the blood was drawn from the heart.
551 Mice were then transcardially perfused with ice-cold sterile PBS. Liver, spleen and brain
552 were collected into sterile plastic bags, and mechanically dissociated. Femur was flushed
553 through a 70 µm cell strainer using 2.5-3 ml sterile PBS in the syringe, and 20 µl of
554 suspension was plated on Granada agar (BD). Skull marrow was extracted as previously
555 described(*12*), with small modifications. After the removal of dura, the calvarium was cut
556 into small pieces into 1 ml sterile PBS using sterile scissors and plated on Granada agar.
557 Dura was incubated for 20 min at 37°C with shaking in 1 ml of sterile RPMI containing
558 2.5 mg of Collagenase IV after which 20 µl of suspension or serial dilution was plated on
559 the Granada agar. To control sterility of the CFU assay, tissues of the control animals were
560 plated in parallel, with no bacterial growth from any analyzed organ.
561
562 **6. Cell extraction**
563 Blood was drawn from the heart. Erythrocytes were lysed in RBC Lysis buffer solution
564 (eBioscience™ 1X RBC Lysis Buffer). The remaining cells were washed in FACS buffer
565 (PBS + 1% FBS + 2 mM EDTA).
566 Dura mater was peeled using forceps from calvaria and placed into a digestion solution
567 (2.5 mg/ml collagenase IV in RPMI) and incubated for 20 min at 37°C shaking, after which
568 the solution was filtered through 70 µm strainer (BD) and washed with FACS buffer.
569 The remaining calvaria was cleaned from leftover muscle and fascia, placed into a 2 ml
570 Eppendorf tube with 1 ml PBS and diced with scissors. The bone marrow was filtered
571 through a 70 µm strainer and washed with FACS buffer.
572 Femur was cleaned from the leftover muscle, and the bone marrow was flushed with PBS
573 using a 26G needle through a 70 µm strainer.
574 Brain was homogenized and filtered through a 100 µm strainer. Myelin was removed using
575 37% Percoll gradient and centrifugation for 30min at 300g RT, with no acceleration and
576 brake.

577 Samples were washed and stained with respective antibodies. FcγII/III receptors were
578 blocked by prior 10 min incubation with Fc block (anti mouse CD16/32 antibody Clone
579 93, Biolegend) on ice.
580 Samples used for bulk RNA-seq (dura and brain) were processed in the same way to avoid
581 potential bias of Mac activation due to enzymatic digestion. Shortly, brain and dura were
582 incubated for 20 min at 37°C shanking in 2.5 mg/ml collagenase IV, after which they were
583 filtered through 70 µm strainer and washed with PBS. The pellet was resuspended using
584 37% Percoll and centrifuged for 30 min at 300g RT, without the acceleration and brake.
585

586 **7. Flow cytometry and FACS**

587 Cells were stained with the indicated antibodies according to manufacturer's instructions.
588 Flow cytometry was performed on a 10-color flow cytometer Gallios™ (Beckman Coulter)
589 or Cytoflex S™ (Beckman Coulter) and FACS was done on Moflo™ (Beckmann Coulter)
590 or CytoFlex™ (Beckman Coulter).
591 The following anti-mouse antibodies were used for surface staining:
592 anti-mouse CD3e APC Clone 145-2C11 (BioLegend)
593 anti-mouse CD16/32 PE Cy7 Clone 93 (eBioscience)
594 anti-mouse CD19 APC Clone 1D3/CD19 (BioLegend)
595 anti-mouse CD34 PE Clone HM34 (BioLegend)
596 anti-mouse CD45 eFluor450 Clone 30-F11 (eBioscience),
597 anti-mouse CD45 FITC Clone 30-F11 (eBioscience)
598 anti-mouse CD45 PerCP Cy5.5 Clone 30-F11 (eBioscience)
599 anti-mouse CD45.1 FITC Clone A20 (eBioscience)
600 anti mouse CD45.2 PerCP Cy5.5 Clone 104 (eBioscience)
601 anti mouse CD11b FITC Clone REA592 (Miltenyi)
602 anti-mouse CD11b PE-Cy7 Clone M1/70 (eBioscience)
603 anti-mouse CD11b APC-eFlour780 Clone M1/70 (eBioscience)
604 anti-mouse CD117 BV421 Clone 2B8 (BioLegend)
605 anti-mouse CD117 PE Cy7 Clone 2B8 (eBioscience)
606 anti-mouse CD115 APC Clone AFS98 (Miltenyi)
607 anti-mouse CD115 BV421 Clone AFS98 (BioLegend)
608 anti-mouse CD127 APC Clone A7R34 (BioLegend)
609 anti-mouse CD206 APC Clone C068C2 (BioLegend)
610 anti-mouse CD206 PE Clone C068C2 (BioLegend)
611 anti-mouse CD206 AF488 Clone C068C2 (BioLegend)
612 anti-mouse CD206 PE Clone C068C2 (BioLegend)
613 anti-mouse CX3CR1 AF488 Clone SA011F11 (BioLegend)
614 anti-mouse Ly6G FITC Clone 1A8 (BD Pharmingen)
615 anti-mouse Ly6G APC Clone 1A8 (BD Pharmingen)
616 anti-mouse Ly6C BV605 Clone HK1.4 (BioLegend)
617 anti-mouse MHC II APC eFlour780 Clone M5/114.15.2 (eBioscience)
618 anti-mouse Ter119 APC Clone TER-119 (BioLegend)
619 anti-mouse Sca-1 AF488 Clone D7 (BioLegend)

620 Analysis was done using Kaluza software (v1.5a and 2.1, Beckman Coulter).
621 For calculating absolute numbers of cells in dura, the whole dura was acquired. For
622 calculating absolute numbers of populations in brain, skull or femur, a defined volume of
623 the processed tissue was acquired for a pre-defined time (30-60s) at a flow of 10 µL/min
624 or 30 µL/min.
625
626 **8. Adoptive transfer**
627 Bone marrow was isolated from tibia and femur of *β-Actin-gfp*$^{+/-}$ mice, flushed with sterile
628 ice-cold PBS and centrifuged for 6 min at 1500 rpm. Cells were resuspended in 1% BSA
629 in PBS, and then stained and sorted as described above. Sorted monocyte progenitors were
630 then resuspended in PBS + 2% murine serum which was obtained from the donor mice.
631 Monocyte progenitors were injected intravenously at 1 dpi (~2–4 × 10^5/animal). Recipients
632 were analyzed 1 day post transfer (2 days post infection). Blood, brain, dura and bone
633 marrow (from femur and skull) were analyzed on a flow cytometer (Gallios™, Beckman
634 Coulter) and processed with the Kaluza software (v2.1, Beckman Coulter) and/or by
635 microscopy.
636
637 **9. RNA extraction and RT-qPCR**
638 Cells were sorted into RLT lysis buffer (Qiagen) with 1% β-mercaptoethanol. RNA was
639 extracted with RNeasy MicroKit (Qiagen) according to the manufacturer's instructions.
640 RNA was reversely transcribed into cDNA using Superscript IV (Invitrogen). RT-qPCR
641 was performed with absolute qPCR SYBR Green Mix (Thermo Fisher Scientific) using
642 Roche Lightcycler™ 175. mRNA levels were normalized to *Gapdh* as housekeeping gene.

Gene	Forward (5'-3')	Reverse (3'-5')
Gapdh	ACTCCACTCACGGCAAATTC	TCTCCATGGTGGTGAAGACA
Ccr2	ACAGCTCAGGATTAACAGGGACTTG	ACCACTTGCATGCACACATGAC

643
644 **10. Bulk RNA sequencing**
645 For bulk RNA sequencing, described populations were sorted into Rneasy Microkit
646 (Qiagen) lysis buffer containing 1% β-mercaptoethanol. RNA was extracted following
647 manufacturer's protocol. To insure appropriate RNA amounts, samples from two mice were
648 pooled for n=1 in both conditions. Bulk RNA sequencing was performed by CeGat
649 (Tübingen, Germany). Sequencing was performed with 2 x 100 bp read length and 50
650 million clusters/probe on NovaSeq 6000 (Illumina). Raw data was provided by CeGat.
651 Group comparison was done using DESeq2 in R. PCA plots were done using DESeq2 in
652 R 4.3.3 and RStudio version 2023.12.1. GO terms were analyzed with the online tool
653 "g:Profiler"(*54*). Heat maps were made using Morpheus
654 (https://software.broadinstitute.org/morpheus).

655
656 **11. Single-cell RNA sequencing**

657 For scRNA Seq of myeloid population, dura mater was prepared from five infected and six
658 control *Wt* mice as described above in section 5.
659 Prior FACS, cells from individual control or infected mice were labelled using the 10X 3'
660 CellPlex Kit Set A (PN-1000261) following manufacturer's recommendations.
661 $CD45^{+}CD11b^{+}$ cell population was sorted. In total, 5-6 individual animals per group were
662 pooled after FACS. For controls, around 10 750 cells were sorted per mouse (64 500 cells
663 in total), and for infected mice, in average 11 600 cells were sorted per mouse (46 400 cells
664 in total). Sorting was done on separate days for control and infected mice due to technical
665 limitations.
666 Sorted samples were processed using the 10X Chromium Next GEM Single Cell 3' Kit
667 v3.1 (PN-1000269) and 3´ Feature Barcode Kit (PN-1000262). Single cell droplets were
668 generated using Chromium Next GEM Chip G Single Cell Kit (PN-1000127) and
669 Chromium Controller for 3' gene expression and cell multiplexing libraries were generated
670 according to the manufacturer's specifications. Library quality was assessed using Agilent
671 TapeStation 4150 Cell-free DNA ScreenTape assay (cat. no. 5067-5630) and NEBNext
672 Library Quant Kit for Illumina (cat. no. E7630S). The single cell libraries were sequenced
673 using Ilumina NextSeq1000/2000, with a minimum targeted sequencing depth of 20,000
674 reads per cell. Fastq files were aligned using the CellRanger version 7.1.
675 For scRNA Seq of MDP-Mo and GMP-Mo, dura from 4 infected $Ms4a3^{Cre};R26^{Tomato}$ mice
676 was processed as described above. Prior FACS, single-cell suspension of each individual
677 mouse was labelled using the 10X 3' CellPlex Kit Set A (PN-1000261) following
678 manufacturer's recommendations. Sorting of MDP-Mo and GMP-Mo was done as
679 described in Fig. S5G. Dump gate included CD206, CD3 and CD19 (all in APC). In total,
680 around 7500 MDP-Mo and 59400 GMP-Mo were sorted. Sorted samples were processed
681 using the 10X Chromium Next GEM Single Cell 3' Kit v3.1 (PN-1000269) and 3´ Feature
682 Barcode Kit (PN-1000262). Single cell droplets were generated using Chromium Next
683 GEM Chip G Single Cell Kit (PN-1000127) and Chromium Controller for 3' gene
684 expression and cell multiplexing libraries were generated according to the manufacturer's
685 specifications. Library quality was assessed using Agilent High Sensitivity DNA Kit (cat.
686 no. 5067-4626). The single cell libraries were sequenced using Ilumina NovaSeq X Plus,
687 with a minimum targeted sequencing depth of 20,000 reads per cell. Fastq files were
688 aligned to prebuilt CellRanger reference refdata-gex-GRCm39-2024-A using the
689 CellRanger version 9.0.1.
690
691 **12. Single-cell RNA sequencing downstream analysis**
692 For myeloid population scSeq from control and infected dura, downstream analyses were
693 conducted in the R version 4.2.0 programming environment using the Seurat package
694 version 4. Cells were retained if the mitochondrial gene content was below 5%. To exclude
695 empty droplets or doublets we limited the number of detected genes per cell between 200
696 and 5,000. Total counts per cell had to exceed 500 to ensure a minimum level of
697 transcriptional activity indicative of viable cells.
698 In addition, we filtered out specific classes of genes that can introduce potential biases by
699 overrepresentation of ribosomal or pseudogenes in the scRNAseq data. Genes belonging

to the murine-specific ribosomal protein large (Gm) family, and ribosomal proteins (Rpl and Rps), were excluded. These genes were identified using regular expressions to match gene names starting with "Gm", "Rpl", or "Rps" and were removed from the analysis.

Data was integrated from two separate experiments using the SCtransform algorithm within Seurat. 2000 features were identified using SelectIntegrationFeatures() and used in PrepSCTIntegration() and FindIntegrationAnchors(). These anchors were used on IntegrateData(). The top 30 PCAs were used for Umap calculation. FindNeighbors() and FindClusters() were calculated with the top 30 dimensions each. For the latter, a resolution of 0.299 was chosen as the highest resolution where every cluster was distinguishable by specific biological functions. Core markers were identified using the FindAllMarkers functions using a threshold of at least 25% of cells expressing the gene and only returning positive values. All clusters are displayed in the respective Violin plots generated by VlnPlot() and sorted according to the respective median.

For monocyte scSeq (GMP-Mo and MDP-Mo), downstream analyses were conducted in R version 4.5.1 programming environment using the Seurat package version 5.3.1. Cells were retained only if the mitochondrial gene content was below 20% and we restricted the number of detected genes per cell to be between 300 and 6,000. Furthermore, total UMI counts per cell were required to exceed 500.

In addition to cell-level filtering, we removed specific classes of genes that could introduce bias due to overrepresentation in scRNA-seq datasets. Genes corresponding to mitochondrial transcripts were identified using the regular expression pattern "(?i)^mt-", and ribosomal protein genes were detected using the pattern "(?i)^(rpl|rps)". To compare transcriptional profiles between MDP-Mo and GMP-Mo populations, pseudobulk function was used, in which counts from individual cells belonging to the same sample and lineage were aggregated to generate sample-level expression profiles. Pseudobulk count matrices were generated for each sample × lineage combination, normalized, and analyzed using DESeq2. DEG were defined as $p<0.05$, logFold2(Change)>0.5. For comparison with bulk RNA seq data from GSE262369, published data was analysed using DESeq2, in which DEG were defined as $p<0.05$, logFold2(Change)>0.5. Heat maps were made using Morpheus (https://software.broadinstitute.org/morpheus).

13. Immunofluorescence labelling

After transcardial perfusion with ice-cold PBS, brain was removed, fixed in 4% PFA for 24 h and cryoprotected in 30% sucrose at 4°C until it sank (1-2 days). After tissue freezing in OCT compound (Sakura, Zoeterwoude, Netherlands) on dry ice, the brain was cut in 30-40 µm sagittal cryosections. Sections were firstly permeabilised for 2h using 0.2% Triton-X in PBS, after which the samples were blocked in blocking solution containing 10% goat serum and 0.1% Triton-X in PBS. Samples were stained with mastermix containing PBS, 5% goat serum, 0.05% Triton-X and antibodies, overnight at 4°C. Dilutions of antibodies were 1:500 for Iba-1 (WACO, Japan), 1:200 for anti-GBS (Invitrogen), 1:100 for CD4 – AF488, CD74 – AF647, CD206 – PE, CD206- APC (Biolegend), 1:100 for CD45-PE (Invitrogen), 1:100 for CD31-PE (BD Pharmigen) and 1:50 for MHC-II APC (Miltenyi). After washing 5x with PBS, samples are incubated for 2h at RT with secondary antibody

743 (goat anti-rabbit Alexa Fluor633 1:500, anti-GFP DyLight488 1:1000 for enhancing
744 endogenous signal in *Cx3Cr1*$^{/gfp}$ mice) and DAPI (1:1000). Samples were washed 5x and
745 mounted on SuperFrost slides using ProLong Diamond Antifade Mountant (Invitrogen).
746 Whole mounts of dura mater were prepared as previously described(*17*), with minor
747 modifications. After transcardial perfusion with ice-cold PBS, calvaria containing cortical
748 dura mater was placed in 4% PFA overnight at 4°C. The dura was dissected and placed into
749 PBS overnight at 4°C to remove any PFA. Samples were then blocked for 2h with agitation
750 on RT using a blocking solution containing 5% goat serum and 0.1% Triton-X. Samples
751 were stained overnight at 4°C in staining solution containing 2% goat serum, 0.1% Triton-
752 X and primary antibodies. Primary antibodies used are as follows: anti-GBS (1:200),
753 CD206 (1:100), CD31 (1:100). Nuclei were stained by DAPI (1:1000).
754 Washing was done 5x with PBS before using the secondary antibodies diluted in a staining
755 solution. Samples were incubated for 2 h at RT. Stained samples were washed thoroughly
756 with PBS and mounted using ProLong Diamond Antifade Mountant.
757 For skull and femur, the tissue was cleaned from muscle and fascia and placed in 4% PFA
758 overnight at 4°C. Next day, the tissues were transferred into decalcification buffer
759 (Osteosoft®, Sigma Aldrich) and shaken for 2 days in a 37°C incubator. The tissues were
760 then washed in PBS and frozen in OCT compound. 15-20 µm cryosections were mounted
761 on gelatin-coated slides. Cuts were rinsed in PBS and washed with PBS with 0.2% Triton
762 X-100 for 30 min, followed by incubation in blocking and permeabilization buffer
763 containing PBS with 0.2% Triton X-100 and 5% normal goat serum for 1 h at RT. Primary
764 antibodies were diluted in 0.05% Triton-X and 2% NGS and incubated at 4°C overnight.
765 The antibody dilutions were: CD45 (1:100), anti-GBS (1:200). Then, sections were washed
766 with PBS 5x, and stained with secondary antibody and DAPI for 2 h at RT. Sections were
767 then washed thoroughly with PBS and mounted using ProLong Diamond Antifade
768 Mountant.
769 Heads were cleared from skin and mandible was removed. Heads were kept in 4% PFA at
770 4°C overnight. Next day, the heads were transferred into decalcification buffer and shaken
771 for 2 days in a 37°C incubator. Heads were then coronally cut with scalpel into
772 approximately 5 mm slices and frozen in OCT compound. 70-80 cryosections were
773 mounted on gelatin-coated slides. The downstream processing and staining was the same
774 as for the brain.
775
776 **14. Confocal microscopy**
777 Confocal microscopy was performed with LSM 880 or LSM 980 confocal microscopes
778 equipped with a 20 × /0.8 NA Plan-Apochromat objective (Carl Zeiss Microimaging) using
779 1-1.5 µm optical slices. Images are displayed as maximum-intensity projections of 25-
780 40µm thick z stacks, 1024x1024 pixel resolution.
781
782 **15. Image analysis**
783 Area and fluorescence intensity were measured using ZEN 3.0 (blue edition, Zeiss). For
784 enumeration of DM per field of view, the pictures were taken on approximately same

785 locations in each dura. CX3CR1-GFP$^+$ DM were manually counted using ImageJ (version
786 1.54p) Cell counter.

787

788 **16. ELISA**

789 For brain ELISA, one brain hemisphere was weighed and stored in 1 ml of homogenization
790 buffer (50 mM Tris pH 8, 150 mM NaCl, 5 mM EDTA) containing 10 µl phosphatase and
791 protease inhibitors (Pierce). Brain was then homogenized using tissue lyser (Quiagen^{TM}
792 TissueLyser) with 50/s oscillations for 5 min with 3 mm tungsten carbide beads. Tissue
793 debris was removed by centrifugation at 20 000 g for 10 min at 4°C. Supernatants were
794 kept at -80°C until the analysis. For plasma ELISA, blood was collected into Microvette®
795 tube (Sarstedt) and centrifuged at 10 000 g for 10 min. Plasma was collected and kept at -
796 80°C until the analysis. Concentrations of IL-6, TNF, IL-1β and IFN-β were measured
797 using mouse R&D Duo set ELISA kits according to the manufacturer's instructions (R&D
798 Systems).

799

800 **17. Statistical analysis**

801 The analysis used for each experiment can be found in figure legends, with the number of
802 replicates and independent experiments. Differences were considered statistically
803 significant if p-values were < 0.05. (ns, not significant; *$p < 0.05$; **$p < 0.01$;
804 ***$p < 0.001$; ****$p < 0.0001$). Data are represented as mean ± SEM if not stated
805 otherwise.
806 GraphPad prism version 10.0.0 was used for statistical analysis.

807

808 **List of supplementary materials:** Supplemental figures 1-6, Supplemental Table 1

809 **References**

810 1. J. Kolter, P. Henneke, Codevelopment of Microbiota and Innate Immunity and the Risk for
811 Group B Streptococcal Disease. *Front. Immunol.* **8**, 1497 (2017).

812 2. M. Kohli-Lynch, N. J. Russell, A. C. Seale, Z. Dangor, C. J. Tann, C. J. Baker, L. Bartlett,
813 C. Cutland, M. G. Gravett, P. T. Heath, M. Ip, K. Le Doare, S. A. Madhi, C. E. Rubens, S.
814 K. Saha, S. Schrag, A. Sobanjo-ter Meulen, J. Vekemans, C. O'Sullivan, F. Nakwa, H. Ben
815 Hamouda, H. Soua, K. Giorgakoudi, S. Ladhani, T. Lamagni, H. Rattue, C. Trotter, J. E.
816 Lawn, Neurodevelopmental Impairment in Children After Group B Streptococcal Disease
817 Worldwide: Systematic Review and Meta-analyses. *Clinical Infectious Diseases* **65**, S190–
818 S199 (2017).

819 3. A. C. Seale, F. Bianchi-Jassir, N. J. Russell, M. Kohli-Lynch, C. J. Tann, J. Hall, L. Madrid,
820 H. Blencowe, S. Cousens, C. J. Baker, L. Bartlett, C. Cutland, M. G. Gravett, P. T. Heath,
821 M. Ip, K. Le Doare, S. A. Madhi, C. E. Rubens, S. K. Saha, S. J. Schrag, A. Sobanjo-ter
822 Meulen, J. Vekemans, J. E. Lawn, Estimates of the Burden of Group B Streptococcal
823 Disease Worldwide for Pregnant Women, Stillbirths, and Children. *Clinical Infectious*
824 *Diseases* **65**, S200–S219 (2017).

825 4. R. Rua, J. Y. Lee, A. B. Silva, I. S. Swafford, D. Maric, K. R. Johnson, D. B. McGavern,
826 Infection drives meningeal engraftment by inflammatory monocytes that impairs CNS
827 immunity. *Nat Immunol* **20**, 407–419 (2019).

828 5. J. Rebejac, E. Eme-Scolan, L. Arnaud Paroutaud, S. Kharbouche, M. Teleman, L. Spinelli,
829 E. Gallo, A. Roussel-Queval, A. Zarubica, A. Sansoni, Q. Bardin, P. Hoest, M.-C. Michallet,
830 C. Brousse, K. Crozat, M. Manglani, Z. Liu, F. Ginhoux, D. B. McGavern, M. Dalod, B.
831 Malissen, T. Lawrence, R. Rua, Meningeal macrophages protect against viral
832 neuroinfection. *Immunity* **55**, 2103-2117.e10 (2022).

833 6. V. Gres, J. Kolter, D. Erny, P. Henneke, The role of CNS macrophages in streptococcal
834 meningoencephalitis. *Journal of Leukocyte Biology* **106**, 209–218 (2019).

835 7. M. Prinz, D. Erny, N. Hagemeyer, Ontogeny and homeostasis of CNS myeloid cells. *Nat*
836 *Immunol* **18**, 385–392 (2017).

837 8. K. Alves De Lima, J. Rustenhoven, J. Kipnis, Meningeal Immunity and Its Function in
838 Maintenance of the Central Nervous System in Health and Disease. *Annu. Rev. Immunol.*
839 **38**, 597–620 (2020).

840 9. H. Van Hove, L. Martens, I. Scheyltjens, K. De Vlaminck, A. R. Pombo Antunes, S. De
841 Prijck, N. Vandamme, S. De Schepper, G. Van Isterdael, C. L. Scott, J. Aerts, G. Berx, G.
842 E. Boeckxstaens, R. E. Vandenbroucke, L. Vereecke, D. Moechars, M. Guilliams, J. A.
843 Van Ginderachter, Y. Saeys, K. Movahedi, A single-cell atlas of mouse brain macrophages
844 reveals unique transcriptional identities shaped by ontogeny and tissue environment. *Nat*
845 *Neurosci* **22**, 1021–1035 (2019).

846 10. J. Rustenhoven, A. Drieu, T. Mamuladze, K. A. De Lima, T. Dykstra, M. Wall, Z.
847 Papadopoulos, M. Kanamori, A. F. Salvador, W. Baker, M. Lemieux, S. Da Mesquita, A.
848 Cugurra, J. Fitzpatrick, S. Sviben, R. Kossina, P. Bayguinov, R. R. Townsend, Q. Zhang,
849 P. Erdmann-Gilmore, I. Smirnov, M.-B. Lopes, J. Herz, J. Kipnis, Functional
850 characterization of the dural sinuses as a neuroimmune interface. *Cell* **184**, 1000-1016.e27
851 (2021).

852 11. J. A. Mazzitelli, L. C. D. Smyth, K. A. Cross, T. Dykstra, J. Sun, S. Du, T. Mamuladze, I.
853 Smirnov, J. Rustenhoven, J. Kipnis, Cerebrospinal fluid regulates skull bone marrow
854 niches via direct access through dural channels. *Nat Neurosci* **25**, 555–560 (2022).

855 12. A. Cugurra, T. Mamuladze, J. Rustenhoven, T. Dykstra, G. Beroshvili, Z. J. Greenberg, W.
856 Baker, Z. Papadopoulos, A. Drieu, S. Blackburn, M. Kanamori, S. Brioschi, J. Herz, L. G.
857 Schuettpelz, M. Colonna, I. Smirnov, J. Kipnis, Skull and vertebral bone marrow are
858 myeloid cell reservoirs for the meninges and CNS parenchyma. *Science* **373**, eabf7844
859 (2021).

860 13. F. E. Pulous, J. C. Cruz-Hernández, C. Yang, Z. Kaya, A. Paccalet, G. Wojtkiewicz, D.
861 Capen, D. Brown, J. W. Wu, M. J. Schloss, C. Vinegoni, D. Richter, M. Yamazoe, M.
862 Hulsmans, N. Momin, J. Grune, D. Rohde, C. S. McAlpine, P. Panizzi, R. Weissleder, D.-E.
863 Kim, F. K. Swirski, C. P. Lin, M. A. Moskowitz, M. Nahrendorf, Cerebrospinal fluid can exit
864 into the skull bone marrow and instruct cranial hematopoiesis in mice with bacterial
865 meningitis. *Nat Neurosci* **25**, 567–576 (2022).

866 14. B. Ajami, J. L. Bennett, C. Krieger, K. M. McNagny, F. M. V. Rossi, Infiltrating monocytes
867 trigger EAE progression, but do not contribute to the resident microglia pool. *Nat Neurosci*
868 **14**, 1142–1149 (2011).

869 15. R. M. Ritzel, A. R. Patel, J. M. Grenier, J. Crapser, R. Verma, E. R. Jellison, L. D.
870 McCullough, Functional differences between microglia and monocytes after ischemic
871 stroke. *J Neuroinflammation* **12**, 1–12 (2015).

872 16. S. Lehnardt, P. Henneke, E. Lien, D. L. Kasper, J. J. Volpe, I. Bechmann, R. Nitsch, J. R.
873 Weber, D. T. Golenbock, T. Vartanian, A Mechanism for Neurodegeneration Induced by
874 Group B Streptococci through Activation of the TLR2/MyD88 Pathway in Microglia. *J*
875 *Immunol* **177**, 583–592 (2006).

876 17. F. A. Pinho-Ribeiro, L. Deng, D. V. Neel, O. Erdogan, H. Basu, D. Yang, S. Choi, A. J.
877 Walker, S. Carneiro-Nascimento, K. He, G. Wu, B. Stevens, K. S. Doran, D. Levy, I. M.
878 Chiu, Bacteria hijack a meningeal neuroimmune axis to facilitate brain invasion. *Nature*
879 **615**, 472–481 (2023).

880 18. M. Djukic, Circulating monocytes engraft in the brain, differentiate into microglia and
881 contribute to the pathology following meningitis in mice. *Brain* **129**, 2394–2403 (2006).

882 19. M. M. Koopmans, J. Engelen-Lee, M. C. Brouwer, V. Jaspers, W. K. Man, M. V. Seron, D.
883 van de Beek, Characterization of a Listeria monocytogenes meningitis mouse model.
884 *Journal of Neuroinflammation* **15** (2018).

885 20. M. N. van Kassel, G. de Boer, S. A. F. Teeri, D. Jamrozy, S. D. Bentley, M. C. Brouwer, A.
886 van der Ende, D. van de Beek, M. W. Bijlsma, Molecular epidemiology and mortality of
887 group B streptococcal meningitis and infant sepsis in the Netherlands: a 30-year
888 nationwide surveillance study. *The Lancet Microbe* **2**, e32–e40 (2021).

889 21. A. Tazi, S. Bellais, I. Tardieux, S. Dramsi, P. Trieu-Cuot, C. Poyart, Group B Streptococcus
890 surface proteins as major determinants for meningeal tropism. *Current Opinion in*
891 *Microbiology* **15**, 44–49 (2012).

892 22. B. Périchon, N. Szili, L. Du Merle, I. Rosinski-Chupin, M. Gominet, S. Bellais, C. Poyart, P.
893 Trieu-Cuot, S. Dramsi, Regulation of PI-2b Pilus Expression in Hypervirulent
894 Streptococcus agalactiae ST-17 BM110. *PLoS ONE* **12**, e0169840 (2017).

895 23. G. Mancuso, A. Midiri, C. Beninati, C. Biondo, R. Galbo, S. Akira, P. Henneke, D.
896 Golenbock, G. Teti, Dual Role of TLR2 and Myeloid Differentiation Factor 88 in a Mouse
897 Model of Invasive Group B Streptococcal Disease. *J Immunol* **172**, 6324–6329 (2004).

898 24. R. Feuerstein, V. Gres, N. Elias Perdigó, S. Baasch, M. Freudenhammer, R. Elling, P.
899 Henneke, Macrophages Are a Potent Source of Streptococcus-Induced IFN-β. *J Immunol*
900 **203**, 3416–3426 (2019).

901 25. M. K. Sharief, M. Ciardi, E. J. Thompson, Blood-Brain Barrier Damage in Patients with
902 Bacterial Meningitis: Association with Tumor Necrosis Factor- but not Interleukin-I. *Journal*
903 *of Infectious Diseases* **166**, 350–358 (1992).

904 26. J. C. Cronk, A. J. Filiano, A. Louveau, I. Marin, R. Marsh, E. Ji, D. H. Goldman, I. Smirnov,
905 N. Geraci, S. Acton, C. C. Overall, J. Kipnis, Peripherally derived macrophages can engraft
906 the brain independent of irradiation and maintain an identity distinct from microglia. *Journal*
907 *of Experimental Medicine* **215**, 1627–1647 (2018).

908 27. F. C. Bennett, M. L. Bennett, F. Yaqoob, S. B. Mulinyawe, G. A. Grant, M. Hayden
909 Gephart, E. D. Plowey, B. A. Barres, A Combination of Ontogeny and CNS Environment
910 Establishes Microglial Identity. *Neuron* **98**, 1170-1183.e8 (2018).

911 28. Y. Werner, E. Mass, P. Ashok Kumar, T. Ulas, K. Händler, A. Horne, K. Klee, A. Lupp, D.
912 Schütz, F. Saaber, C. Redecker, J. L. Schultze, F. Geissmann, R. Stumm, Cxcr4
913 distinguishes HSC-derived monocytes from microglia and reveals monocyte immune
914 responses to experimental stroke. *Nat Neurosci* **23**, 351–362 (2020).

915 29. Y. Huang, Z. Xu, S. Xiong, F. Sun, G. Qin, G. Hu, J. Wang, L. Zhao, Y.-X. Liang, T. Wu, Z.
916 Lu, M. S. Humayun, K.-F. So, Y. Pan, N. Li, T.-F. Yuan, Y. Rao, B. Peng, Repopulated
917 microglia are solely derived from the proliferation of residual microglia after acute
918 depletion. *Nat Neurosci* **21**, 530–540 (2018).

919 30. T. Goldmann, P. Wieghofer, M. J. C. Jordão, F. Prutek, N. Hagemeyer, K. Frenzel, L.
920 Amann, O. Staszewski, K. Kierdorf, M. Krueger, G. Locatelli, H. Hochgerner, R. Zeiser, S.
921 Epelman, F. Geissmann, J. Priller, F. M. V. Rossi, I. Bechmann, M. Kerschensteiner, S.
922 Linnarsson, S. Jung, M. Prinz, Origin, fate and dynamics of macrophages at central
923 nervous system interfaces. *Nat Immunol* **17**, 797–805 (2016).

924 31. C. Blériot, T. Dupuis, G. Jouvion, G. Eberl, O. Disson, M. Lecuit, Liver-Resident
925 Macrophage Necroptosis Orchestrates Type 1 Microbicidal Inflammation and Type-2-
926 Mediated Tissue Repair during Bacterial Infection. *Immunity* **42**, 145–158 (2015).

927 32. N. Robinson, S. McComb, R. Mulligan, R. Dudani, L. Krishnan, S. Sad, Type I interferon
928 induces necroptosis in macrophages during infection with Salmonella enterica serovar
929 Typhimurium. *Nat Immunol* **13**, 954–962 (2012).

930 33. S. Brioschi, W.-L. Wang, V. Peng, M. Wang, I. Shchukina, Z. J. Greenberg, J. K. Bando, N.
931 Jaeger, R. S. Czepielewski, A. Swain, D. A. Mogilenko, W. L. Beatty, P. Bayguinov, J. A. J.
932 Fitzpatrick, L. G. Schuettpelz, C. C. Fronick, I. Smirnov, J. Kipnis, V. S. Shapiro, G. F. Wu,
933 S. Gilfillan, M. Cella, M. N. Artyomov, S. H. Kleinstein, M. Colonna, Heterogeneity of
934 meningeal B cells reveals a lymphopoietic niche at the CNS borders. *Science*, doi:
935 10.1126/science.abf9277 (2021).

936 34. A. Mildner, H. Schmidt, M. Nitsche, D. Merkler, U.-K. Hanisch, M. Mack, M. Heikenwalder,
937 W. Brück, J. Priller, M. Prinz, Microglia in the adult brain arise from Ly-6ChiCCR2+
938 monocytes only under defined host conditions. *Nat Neurosci* **10**, 1544–1553 (2007).

939 35. F. Geissmann, S. Jung, D. R. Littman, Blood Monocytes Consist of Two Principal Subsets
940 with Distinct Migratory Properties. *Immunity* **19**, 71–82 (2003).

941 36. J. W. Swann, O. C. Olson, E. Passegué, Made to order: emergency myelopoiesis and
942 demand-adapted innate immune cell production. *Nat Rev Immunol* **24**, 596–613 (2024).

943 37. A. Yáñez, S. G. Coetzee, A. Olsson, D. E. Muench, B. P. Berman, D. J. Hazelett, N.
944 Salomonis, H. L. Grimes, H. S. Goodridge, Granulocyte-Monocyte Progenitors and
945 Monocyte-Dendritic Cell Progenitors Independently Produce Functionally Distinct
946 Monocytes. *Immunity* **47**, 890-902.e4 (2017).

947 38. Z. Liu, Y. Gu, S. Chakarov, C. Bleriot, I. Kwok, X. Chen, A. Shin, W. Huang, R. J. Dress,
948 C.-A. Dutertre, A. Schlitzer, J. Chen, L. G. Ng, H. Wang, Z. Liu, B. Su, F. Ginhoux, Fate
949 Mapping via Ms4a3-Expression History Traces Monocyte-Derived Cells. *Cell* **178**, 1509-
950 1525.e19 (2019).

951 39. S. Trzebanski, J.-S. Kim, N. Larossi, A. Raanan, D. Kancheva, J. Bastos, M. Haddad, A.
952 Solomon, E. Sivan, D. Aizik, J. S. Kralova, M. Gross-Vered, S. Boura-Halfon, T. Lapidot, R.
953 Alon, K. Movahedi, S. Jung, Classical monocyte ontogeny dictates their functions and fates
954 as tissue macrophages. *Immunity*, S1074-7613(24)00224–3 (2024).

955 40. L. M. Harden, S. Leahy, S. G. Lala, P. Paul, J. Chandna, S. Lowick, S. Mbatha, T. Jaye, B.
956 Laughton, A. Ghoor, P. Sithole, J. Msayi, N. Kumalo, T. N. Msibi, S. A. Madhi, J. E. Lawn,
957 Z. Dangor, South African Children: A Matched Cohort Study of Neurodevelopmental
958 Impairment in Survivors of Invasive Group B *Streptococcus* Disease Aged 5 to 8 Years.
959 *Clinical Infectious Diseases* **74**, S5–S13 (2022).

960 41. J. V. Forrester, P. G. McMenamin, S. J. Dando, CNS infection and immune privilege. *Nat*
961 *Rev Neurosci* **19**, 655–671 (2018).

962 42. J. S. Braun, J. E. Sublett, D. Freyer, T. J. Mitchell, J. L. Cleveland, E. I. Tuomanen, J. R.
963 Weber, Pneumococcal pneumolysin and H_2O_2 mediate brain cell apoptosis during
964 meningitis. *J Clin Invest* **109**, 19–27 (2002).

965 43. J. Zweigner, S. Jackowski, S. H. Smith, M. van der Merwe, J. R. Weber, E. I. Tuomanen,
966 Bacterial Inhibition of Phosphatidylcholine Synthesis Triggers Apoptosis in the Brain. *J Exp*
967 *Med* **200**, 99–106 (2004).

968 44. A. J. Schain, A. Melo-Carrillo, D. Borsook, J. Grutzendler, A. M. Strassman, R. Burstein,
969 Activation of pial and dural macrophages and dendritic cells by cortical spreading
970 depression. *Annals of Neurology* **83**, 508–521 (2018).

971 45. F. Herisson, V. Frodermann, G. Courties, D. Rohde, Y. Sun, K. Vandoorne, G. R.
972 Wojtkiewicz, G. S. Masson, C. Vinegoni, J. Kim, D.-E. Kim, R. Weissleder, F. K. Swirski,
973 M. A. Moskowitz, M. Nahrendorf, Direct vascular channels connect skull bone marrow and
974 the brain surface enabling myeloid cell migration. *Nat Neurosci* **21**, 1209–1217 (2018).

975 46. Z. I. Kolabas, L. B. Kuemmerle, R. Perneczky, B. Förstera, S. Ulukaya, M. Ali, S. Kapoor,
976 L. M. Bartos, M. Büttner, O. S. Caliskan, Z. Rong, H. Mai, L. Höher, D. Jeridi, M. Molbay, I.
977 Khalin, I. K. Deligiannis, M. Negwer, K. Roberts, A. Simats, O. Carofiglio, M. I. Todorov, I.
978 Horvath, F. Ozturk, S. Hummel, G. Biechele, A. Zatcepin, M. Unterrainer, J. Gnörich, J.
979 Roodselaar, J. Shrouder, P. Khosravani, B. Tast, L. Richter, L. Díaz-Marugán, D.
980 Kaltenecker, L. Lux, Y. Chen, S. Zhao, B.-S. Rauchmann, M. Sterr, I. Kunze, K. Stanic, V.
981 W. Y. Kan, S. Besson-Girard, S. Katzdobler, C. Palleis, J. Schädler, J. C. Paetzold, S.
982 Liebscher, A. E. Hauser, O. Gokce, H. Lickert, H. Steinke, C. Benakis, C. Braun, C. P.
983 Martinez-Jimenez, K. Buerger, N. L. Albert, G. Höglinger, J. Levin, C. Haass, A. Kopczak,
984 M. Dichgans, J. Havla, T. Kümpfel, M. Kerschensteiner, M. Schifferer, M. Simons, A. Liesz,

N. Krahmer, O. A. Bayraktar, N. Franzmeier, N. Plesnila, S. Erener, V. G. Puelles, C. Delbridge, H. S. Bhatia, F. Hellal, M. Elsner, I. Bechmann, B. Ondruschka, M. Brendel, F. J. Theis, A. Erturk, Distinct molecular profiles of skull bone marrow in health and neurological disorders. *Cell* **186**, 3706-3725.e29 (2023).

47. Z. Fitzpatrick, N. G. Zanluqui, J. S. Rosenblum, Z. K. Tuong, C. Y. C. Lee, V. Chandrashekhar, M. L. Negro-Demontel, A. P. Stewart, D. A. Posner, M. Buckley, K. S. J. Allinson, P. Mastorakos, P. Chittiboina, D. Maric, D. Donahue, A. Helmy, T. Tajsic, J. R. Ferdinand, A. Portet, A. Peñalver, E. Gillman, Z. Zhuang, M. R. Clatworthy, D. B. McGavern, Venous-plexus-associated lymphoid hubs support meningeal humoral immunity. *Nature* **628**, 612–619 (2024).

48. L. Amann, A. Fell, G. Monaco, R. Sankowski, H. Z. Q. Wu, M. J. C. Jordão, K. Borst, M. Fliegauf, T. Masuda, A. Ardura-Fabregat, N. Paterson, E. Nent, J. Cook, O. Staszewski, O. Mossad, T. Falk, A. Louveau, I. Smirnov, J. Kipnis, T. Lämmermann, M. Prinz, Extrasinusoidal macrophages are a distinct subset of immunologically active dural macrophages. *Science Immunology*, doi: 10.1126/sciimmunol.adh1129 (2024).

49. M. W. Barth, J. A. Hendrzak, M. J. Melnicoff, P. S. Morahan, Review of the macrophage disappearance reaction. *Journal of Leukocyte Biology* **57**, 361–367 (1995).

50. P. A. Louwe, L. Badiola Gomez, H. Webster, G. Perona-Wright, C. C. Bain, S. J. Forbes, S. J. Jenkins, Recruited macrophages that colonize the post-inflammatory peritoneal niche convert into functionally divergent resident cells. *Nat Commun* **12**, 1–15 (2021).

51. S. M. Lai, J. Sheng, P. Gupta, L. Renia, K. Duan, F. Zolezzi, K. Karjalainen, E. W. Newell, C. Ruedl, Organ-Specific Fate, Recruitment, and Refilling Dynamics of Tissue-Resident Macrophages during Blood-Stage Malaria. *Cell Reports* **25**, 3099-3109.e3 (2018).

52. B. J. Kim, M. A. McDonagh, L. Deng, B. D. Gastfriend, A. Schubert-Unkmeir, K. S. Doran, E. V. Shusta, Streptococcus agalactiae disrupts P-glycoprotein function in brain endothelial cells. *Fluids Barriers CNS* **16**, 26 (2019).

53. K. S. Doran, E. J. Engelson, A. Khosravi, H. C. Maisey, I. Fedtke, O. Equils, K. S. Michelsen, M. Arditi, A. Peschel, V. Nizet, Blood-brain barrier invasion by group B *Streptococcus* depends upon proper cell-surface anchoring of lipoteichoic acid. *J Clin Invest* **115**, 2499–2507 (2005).

54. L. Kolberg, U. Raudvere, I. Kuzmin, P. Adler, J. Vilo, H. Peterson, g:Profiler—interoperable web service for functional enrichment analysis and gene identifier mapping (2023 update). *Nucleic Acids Research* **51**, W207–W212 (2023).

Acknowledgments: We thank Anita Imm, Reem Alsumati, Adriana Greco and Lena Grubišić for their great technical assistance. We thank the ZTZ core facility, especially Jan Bodinek and Marie Follo for their great technical assistance. We thank the Center for Experimental Models and Transgenic Service (CEMT) of University Medical Center Freiburg for excellent technical support and assistance with the animal studies performed in this work. We thank Pedro Aniceto for his assistance with analysis in R and R Studio.

Funding: AL and FL were supported by the IMM-PACT clinician scientist programme, funded by the Deutsche Forschungsgesellschaft (DFG, German Research Foundation) – 413517907. PH, MP, KK, JK, S, JK and DE received funding the via TRR359 (DFG, project ID 491676693); MP, SJ, KK, AL, DE and PH received funding via TRR167 (project ID 259373024); MP, KK and PH were funded via CRC1160 (DFG, project ID 256073931). PH received further support from the DFG (HE3127/9, HE3127/12, HE3127/16). DE was further supported by the Berta-Ottenstein-Programme for advanced Clinician Scientists, the Else Kröner-Fresenius-Stiftung and Ministry of Science, Research and Arts, Baden-Wuerttemberg under the aegis of JPND. This study was supported in part by the Excellence Initiative of the German Research Foundation (GSC-4, Spemann Graduate School) and in part by the Ministry for Science, Research and Arts of the State of Baden-Württemberg.

Author contributions:

Conceptualization: PH, VG

Supervision: PH, DE

Formal analysis: VG, FL, LFPB, GM, S, DO

Investigation: VG, VF, AL, JN, ZMM, TM, SB, JH

Resources: PH, KPK, MP, SJ

Validation: VG, JK

Visualization: VG

Writing – original draft: VG, PH

Writing – review and editing: PH, KK, JK, DE, S, FL, AL, JK, SB, VF, JN, ZMM

Competing interests: Authors declare that they have no competing interests.

Data and materials availability: Please contact the first (VG) or corresponding author (PH) if you want an access to the transcriptome data generated in this study or other information not covered in the method section.

Fig. 1

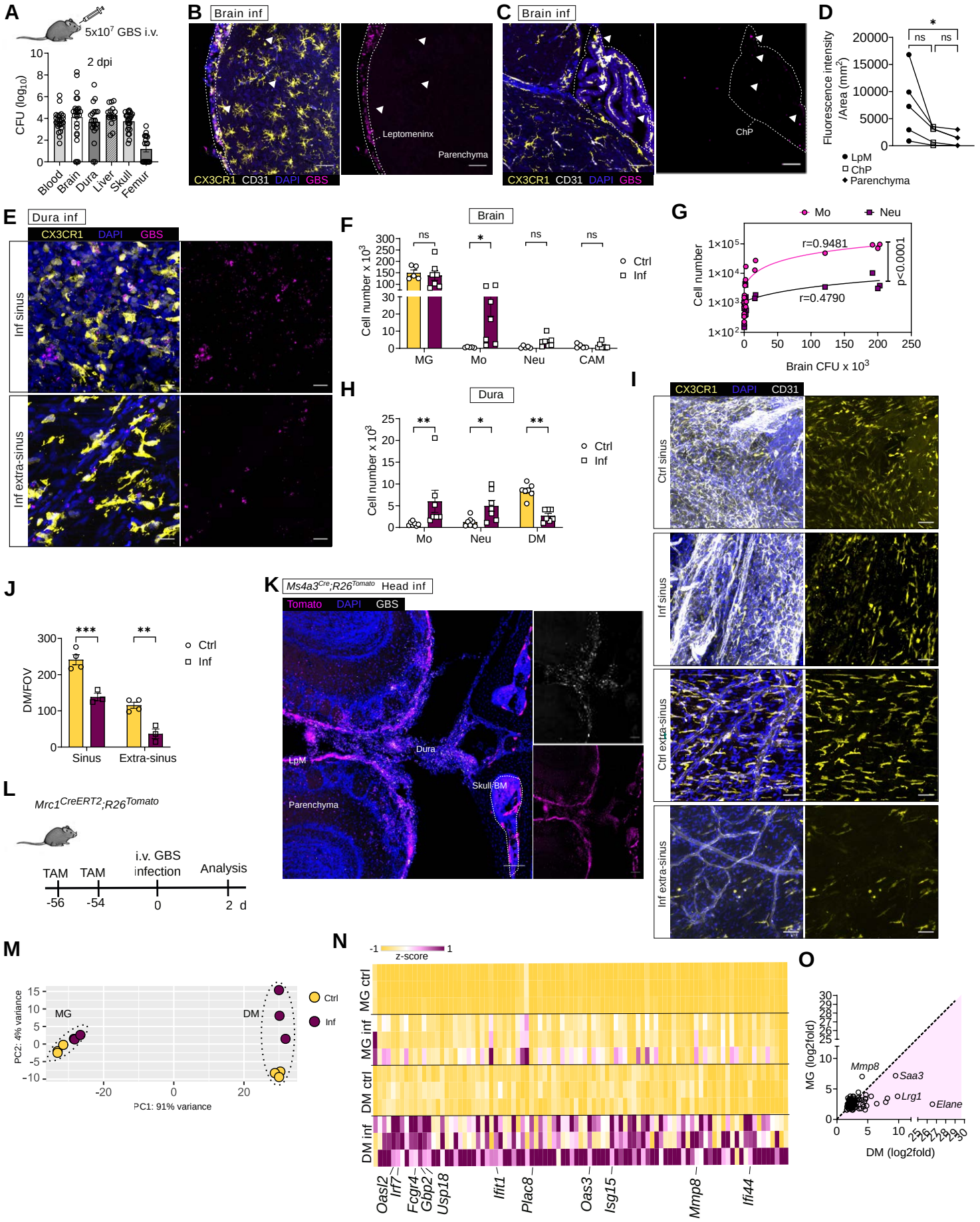
A
5x10^7 GBS i.v.
2 dpi
CFU (log10)
Blood
Brain
Dura
Liver
Skull
Femur
B
Brain inf
Leptomeninx
Parenchyma
CX3CR1 CD31 DAPI GBS
C
Brain inf
ChP
CX3CR1 CD31 DAPI GBS
D
Fluorescence intensity /Area (mm²)
ns
ns
LpM
ChP
Parenchyma
E
Dura inf
CX3CR1 DAPI GBS
Inf sinus
Inf extra-sinus
F
Brain
Cell number x 10³
Ctrl
Inf
MG
Mo
Neu
CAM
G
Mo
Neu
Cell number
r=0.9481
r=0.4790
p<0.0001
Brain CFU x 10³
H
Dura
Cell number x 10³
Ctrl
Inf
Mo
Neu
DM
I
CX3CR1 DAPI CD31
Ctrl sinus
Inf sinus
Ctrl extra-sinus
Inf extra-sinus
J
DM/FOV
Ctrl
Inf
Sinus
Extra-sinus
K
Ms4a3Cre;R26Tomato Head inf
Tomato DAPI GBS
LpM
Dura
Skull/BM
Parenchyma
L
Mrc1CreERT2;R26Tomato
TAM
TAM
i.v. GBS infection
Analysis
-56
-54
0
2 d
M
PC2: 4% variance
PC1: 91% variance
MG
DM
Ctrl
Inf
N
z-score
MG ctrl
MG inf
DM ctrl
DM inf
Oasl2
Irf7
Fcgr4
Gbp2
Usp18
Ifit1
Plac8
Oas3
Isg15
Mmp8
Ifi44
O
MG (log2fold)
DM (log2fold)
Mmp8
Saa3
Lrg1
Elane

Fig. 1: Hematogenous GBS infection highlights the meninges as a reactive CNS barrier

A: *Wt* mice were intravenously injected with $5x10^7$ CFU of the serotype III hypervirulent BM110 GBS strain. Colony forming units (CFU) counts from homogenized brains (n=25), dura (n=21), liver (n=16), extracted bone marrow from femur (n=19) and skull (n=25) (per tissue/organ) and blood culture (per ml) (n=24) at 2 dpi. Data represent at least five independent experiments.

B-C: Representative maximal intensity projection of sagittal brain slices of infected *Cx3cr1*$^{gfp/+}$ mice including leptomeningeal area and parenchyma (**B**) and choroid plexus (ChP) (**C**) labelled with GBS-AF633 (magenta) and DAPI (blue). White arrows mark some of the GBS found in the parenchyma and choroid plexus. Scale bar = 50 µm.

D: Fluorescence intensity of GBS-AF633 labelling divided by the area of leptomeninges (LpM), cortical parenchyma, or choroid plexus (ChP). For ChP, either the lateral or the third ventricle was imaged. Each dot represents an individual infected mouse, n=5. Statistics by paired t-test. *p<0.05, data represents at least three independent experiments.

E: Representative maximal intensity projection of dural whole mount from infected *Cx3cr1*$^{gfp/+}$ mice labelled with GBS-AF633 (magenta) and DAPI (blue), from either region of the sinus or the extra-sinus region. Scale bar = 20 µm.

F: Absolute numbers of microglia (MG), monocytes (Mo), neutrophils (Neu) and CNS-associated macrophages (CAM), including leptomeningeal, perivascular and choroid plexus Macs from control (Ctrl) and infected (Inf) mice measured by flow cytometry. One brain hemisphere per mouse was used for quantification. n=5-7, data represents at least two independent experiments. Multiple Mann-Whitney test followed by Holm-Šídák, *p<0.05, ns = not significant

G: Correlation of CFU counts and total monocyte or neutrophil number in the brain assessed by Spearman correlation. Slopes compared by simple linear regression, n=20. Data represent at least three independent experiments. R represents the goodness of fit in simple linear regression. p<0.0001

H: Absolute numbers of monocytes, neutrophils and DM from control and infected dura mater measured by flow cytometry, n=7. Statistics by Multiple Mann-Whitney test followed by Holm-Šídák. Data represent at least two independent experiments. *p<0.05, **p <0.01.

I: Representative maximal intensity projection of dural whole mount from control and infected *Cx3cr1*$^{gfp/+}$ mice stained with DAPI (blue) and labelled with CD31-PE (white) showing loss of GFP-positive DM, in sinus and extra-sinus area. Scale bar = 50 µm.

J: Quantification of *Cx3cr1*$^{gfp/+}$ DM per field of view (FOV) in sinus and extra-sinus area of control and infected dura. 2-3 sinus and extra-sinus positions were quantified per mouse, and average values were plotted. N= 3-4, from two independent experiments. Statistics by two-way ANOVA, followed by Tukey's multiple comparisons test. **p<0.01, ***p <0.001

K: Representative image of a coronal slice of infected *Ms4a3*^{Cre}*;R26*^{Tomato} mouse head, stained with DAPI (blue), and labelled with GBS-AF633 (white). Scale bar = 100 µm.

L: Scheme of experimental time course. *Mrc1*^{CreERT2};*R26*^{Tomato} mice were treated with tamoxifen twice, 8 weeks prior to the infection. At 2 dpi, DM and MG were sorted from dura and brain. Two mice were pooled for n=1, in total 6 mice were used (n=3).

M: Principal component analysis (PCA) of bulk RNA-seq from sorted populations.

N: Z-score heat map of 93 common upregulated DEG in both MG and DM, with $\log_2$(fold change) larger than 1.5 and padj<0.05.

O: A comparison scatter plot of genes upregulated both in MG and DM, shown as a $\log_2$(fold change) of common upregulated DEG from MG and DM.

Fig. 2

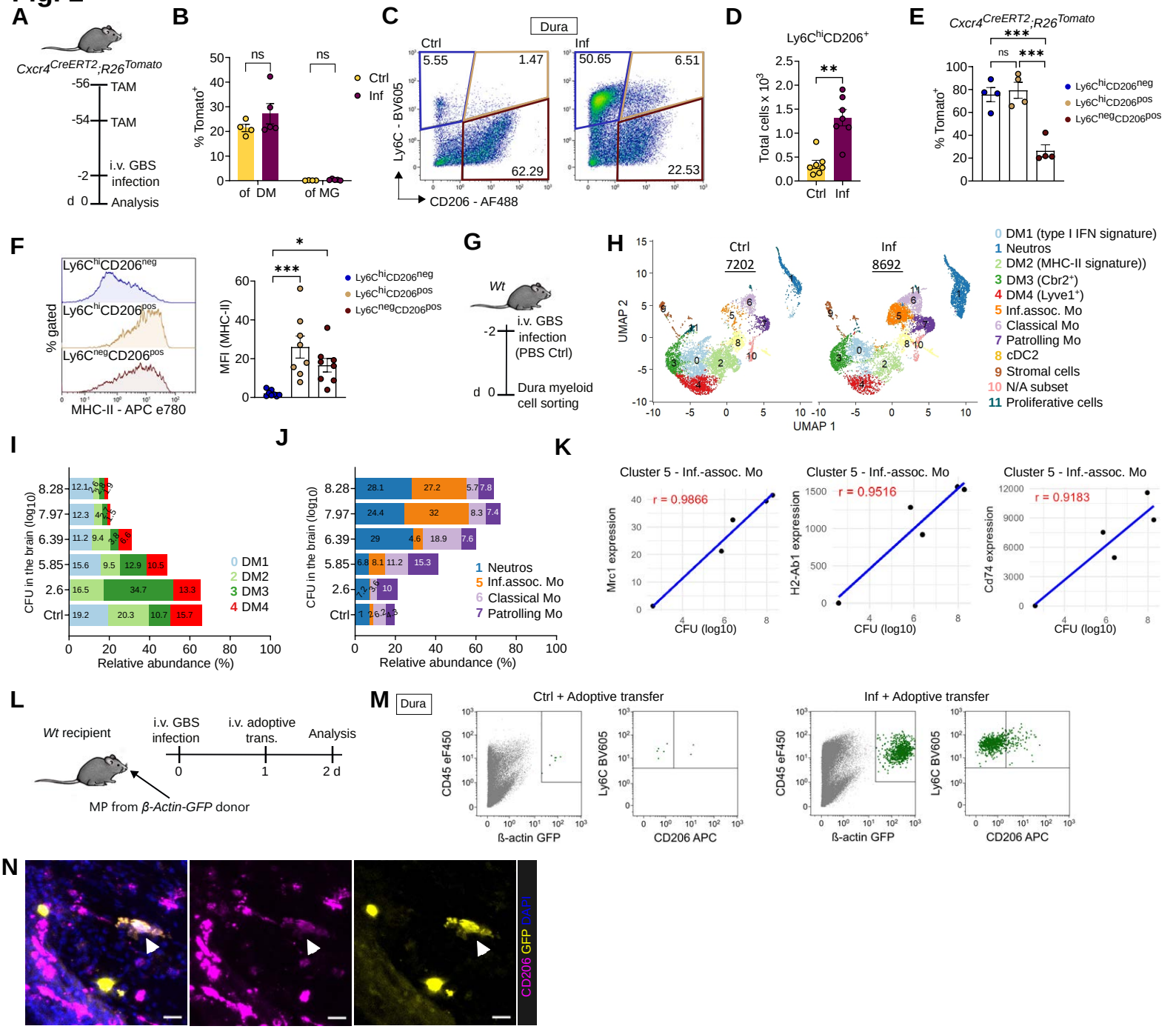
A
Cxcr4CreERT2;R26Tomato
-56 TAM
-54 TAM
-2 i.v. GBS infection
d 0 Analysis
B
% Tomato+
ns
ns
Ctrl
Inf
of DM
of MG
C
Dura
Ctrl
Inf
5.55
1.47
62.29
50.65
6.51
22.53
Ly6C - BV605
CD206 - AF488
D
Ly6ChiCD206+
Total cells x 10^3
**
Ctrl
Inf
E
Cxcr4CreERT2;R26Tomato
***
ns
***
% Tomato+
Ly6ChiCD206neg
Ly6ChiCD206pos
Ly6CnegCD206pos
F
Ly6ChiCD206neg
Ly6ChiCD206pos
Ly6CnegCD206pos
% gated
MHC-II - APC e780
MFI (MHC-II)
*
***
G
Wt
-2 i.v. GBS infection (PBS Ctrl)
d 0 Dura myeloid cell sorting
H
Ctrl
7202
Inf
8692
UMAP 2
UMAP 1
0 DM1 (type I IFN signature)
1 Neutros
2 DM2 (MHC-II signature))
3 DM3 (Cbr2+)
4 DM4 (Lyve1+)
5 Inf.assoc. Mo
6 Classical Mo
7 Patrolling Mo
8 cDC2
9 Stromal cells
10 N/A subset
11 Proliferative cells
I
CFU in the brain (log10)
8.28
7.97
6.39
5.85
2.6
Ctrl
0 DM1
2 DM2
3 DM3
4 DM4
Relative abundance (%)
J
CFU in the brain (log10)
1 Neutros
5 Inf.assoc. Mo
6 Classical Mo
7 Patrolling Mo
Relative abundance (%)
K
Cluster 5 - Inf.-assoc. Mo
r = 0.9866
Mrc1 expression
CFU (log10)
Cluster 5 - Inf.-assoc. Mo
r = 0.9516
H2-Ab1 expression
CFU (log10)
Cluster 5 - Inf.-assoc. Mo
r = 0.9183
Cd74 expression
CFU (log10)
L
Wt recipient
i.v. GBS infection
i.v. adoptive trans.
Analysis
0
1
2 d
MP from β-Actin-GFP donor
M
Dura
Ctrl + Adoptive transfer
Inf + Adoptive transfer
CD45 eF450
ß-actin GFP
Ly6C BV605
CD206 APC
N
CD206 GFP DAPI

Fig. 2: Loss of dural macrophages triggers compensatory monocyte differentiation

A: Scheme of experimental timeline. *Cxcr4*$^{CreERT2;}$*R26*^{Tomato} mice were induced with tamoxifen (TAM) 8 weeks prior to GBS infection and sacrificed at 2 dpi.

B: Percentages of Tomato-labelled CD45^{hi}CD11b^{+}Ly6C^{neg}Ly6G^{neg}CD206^{+} DM in dura and CD45^{lo}CD11b^{+}Ly6C^{neg}Ly6G^{neg}CD206^{neg} MG in brain. Statistic by Mann-Whitney U-test n=4-5. Data represent three independent experiments. ns=not significant.

C: Representative flow cytometry plots showing a presence of Ly6C^{hi}CD206^{+} population in infected and control mice. Numbers in each gate indicate the percentage of the population.

D: Flow cytometry-based quantification of Ly6C^{hi}CD206^{+} population in Ctrl and Inf mice, n=7 Statistics by Mann-Whitney U-test. Data represent three independent experiments. **p<0.01

E: Percentage of Tomato-labeling in *Cxcr4*$^{CreERT2;}$*R26*^{Tom} mice in Ly6C^{hi}CD206^{+} population in comparison to Ly6C^{hi}CD206^{neg} monocytes and Ly6C^{neg}CD206^{+} DM in infected dura. n=4, representing two independent experiments. Statistics by ordinary one-way ANOVA, followed by Dunnett's multiple comparisons test. ns= not significant, ***p<0.001

F: MHC-II expression in Ly6C^{hi}CD206^{+} population in comparison to Ly6C^{hi}CD206^{neg} monocytes and Ly6C^{neg}CD206^{+} DM. MHC-II expression is visualized as mean intensity fluorescence (MFI). n=8, representing three independent experiments. Statistics by ordinary one-way ANOVA, followed by Tukey's multiple comparisons test. *p<0.05, ***p<0.001.

G: Scheme of experimental timeline used for sorting of myeloid population for single cell sequencing.

H: Uniform Manifold Approximation and Projection (UMAP) representation based on gene expression profiling of sorted CD45^{+}CD11b^{+} myeloid population from the control and infected dura of *Wt* mice. The number of analyzed cells per condition is underlined.

I: Relative abundance of DM clusters (0, 2, 3, 4) expressed as percentages of total myeloid cells, according to the individual bacterial burden in the brain, or the overall percentages from control mice. Each color represents a specific cluster indicated in **H**.

J: Relative abundance of neutrophil and monocyte clusters (1, 5, 6, 7) expressed as percentages of total myeloid cells, according to the individual bacterial burden in the brain, or the overall percentages from control mice. Each color represents a specific cluster indicated in **H**.

K: Linear regression of *Mrc1*, *H2-Ab1* and *Cd74* expression in infection-associated monocytes (cluster 5) against GBS CFU counts in the brain. To calculate R, Pearson correlation coefficient was used between its average expression level and the CFU count of the respective replicate.

L: Scheme of experimental setup for adoptive transfer experiment. *Wt* mice were infected and 1 dpi received 2-4x10^{5} monocyte progenitors (MP) sorted from bone marrows *of β-Actin-GFP* mice. Control mice were administered with PBS before receiving transferred monocyte progenitors**.**

M: Flow cytometry plots showing partial upregulation of CD206 in donor *β-Actin-GFP* mice bone marrow monocyte progenitors transferred to infected *Wt* mice.

N: Representative image of infected dura, a *β-Actin-GFP* mice bone marrow donor-derived monocyte progenitor upregulating CD206 is marked with arrow. Scale bar = 20 µm.

Fig. 3

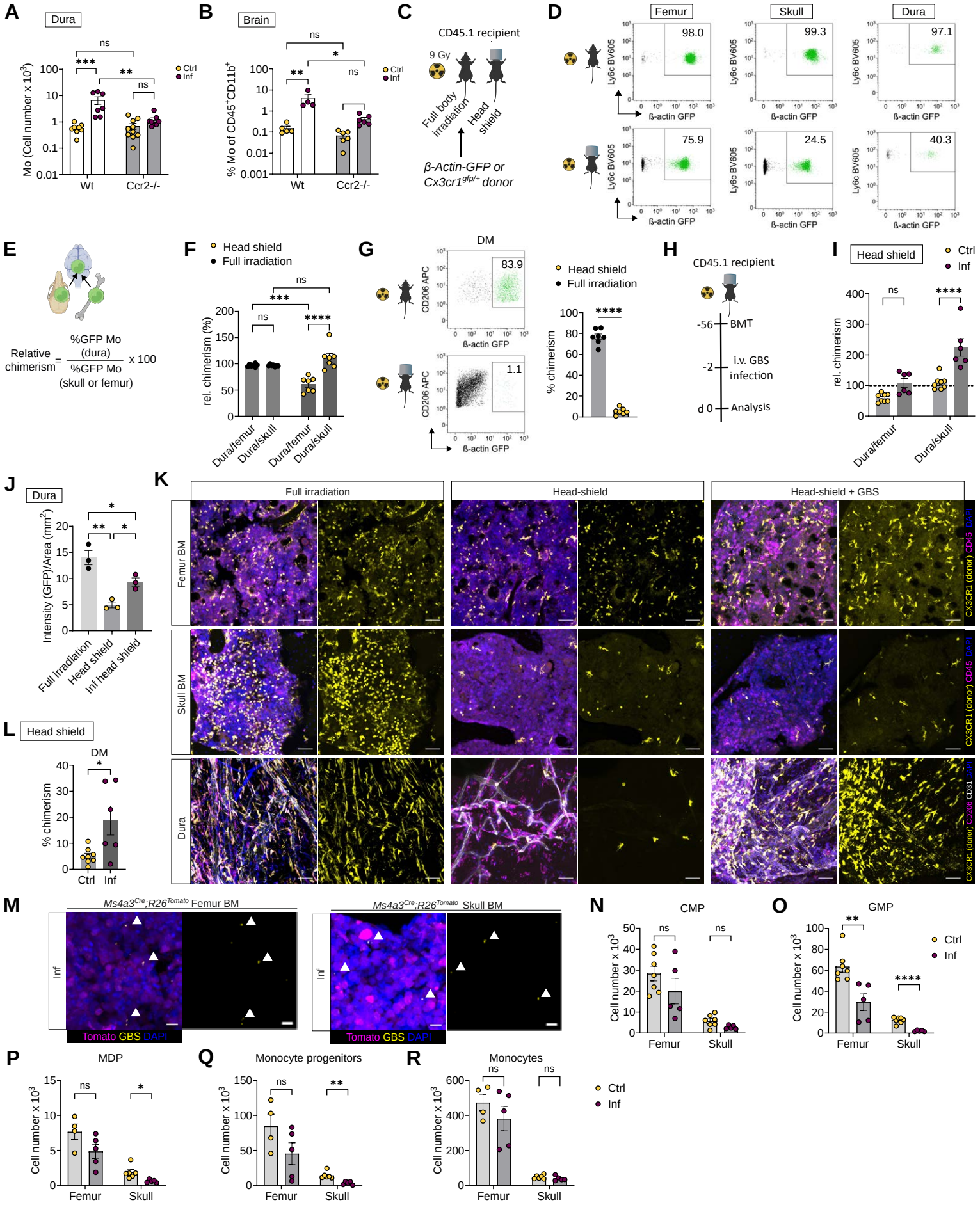
A
Dura
Mo (Cell number x 10^3)
Ctrl
Inf
Wt
Ccr2-/-
B
Brain
% Mo of CD45+CD11b+
C
CD45.1 recipient
9 Gy
Full body irradiation
Head shield
β-Actin-GFP or Cx3cr1gfp/+ donor
D
Femur
Skull
Dura
98.0
99.3
97.1
75.9
24.5
40.3
Ly6c BV605
ß-actin GFP
E
Relative chimerism = %GFP Mo (dura) / %GFP Mo (skull or femur) x 100
F
Head shield
Full irradiation
rel. chimerism (%)
Dura/femur
Dura/skull
G
DM
83.9
1.1
CD206 APC
ß-actin GFP
% chimerism
H
CD45.1 recipient
-56 BMT
-2 i.v. GBS infection
d 0 Analysis
I
Head shield
rel. chimerism
J
Dura
Intensity (GFP)/Area (mm2)
Full irradiation
Head shield
Inf head shield
K
Full irradiation
Head-shield
Head-shield + GBS
Femur BM
Skull BM
Dura
CX3CR1 (donor) CD45 DAPI
CX3CR1 (donor) CD206 CD31 DAPI
L
Head shield
DM
% chimerism
Ctrl
Inf
M
Ms4a3Cre;R26Tomato Femur BM
Ms4a3Cre;R26Tomato Skull BM
Inf
Tomato GBS DAPI
N
CMP
Cell number x 10^3
Femur
Skull
O
GMP
P
MDP
Q
Monocyte progenitors
R
Monocytes

Fig. 3: Distinct monocyte sources support dural immunity in steady state and infection

A: Flow cytometry quantitative analysis of monocytes from dura of control and infected *Wt* or *Ccr2*$^{-/-}$ mice. n=7-10, from at least three independent experiments. Statistics by two-way ANOVA and Tukey's multiple comparisons test **p<0.01, ***p<0.001, ns=not significant.

B: Flow cytometry analysis of monocyte frequencies from the brains of control and infected *Wt* or *Ccr2*$^{-/-}$ mice. n=4-6, from at least two independent experiments. Statistics by two-way ANOVA and Tukey's multiple comparisons test, *p<0.05, **p<0.01, ns=not significant.

C: Scheme of different strategies of radiation procedure followed by bone marrow transplantation from *Cx3cr1*$^{+/gfp}$ or *β-Actin-GFP* mice. Analysis was done 8 weeks post bone marrow transfer.

D: Representative flow cytometry plots depicting donor-originating monocytes in green, from either fully irradiated mice or head-shielded mice. Numbers in gates represent % of gated GFP-positive (donor-derived) monocytes.

E: Scheme of calculation of relative chimerism with formula used. Illustration made in BioRender (biorender.com). Monocytes= Mo.

F: Chimerism rates of monocytes in dura compared to chimerism of skull monocytes, or femur monocytes. Statistics by two-way ANOVA followed by Tukey's multiple comparisons test. n=7, data represent at least three independent experiments. ***p<0.001, ****p<0.0001, ns=not significant.

G: On the left, representative flow cytometry plots depicting donor-originating DM in green, from either fully irradiated mice or head-shielded mice. Numbers in gates represent % of gated GFP-positive (donor-derived) DM. On the right, chimerism rates of DM in fully irradiated or head-shielded mice. Statistics by Mann-Whitney U – test. n=7, data represent three independent experiments. ****p<0.0001.

H: Scheme of experimental timeline post head-shielded irradiation. 8 weeks post head-shielded irradiation and bone marrow transfer (BTM), mice were infected with GBS and analyzed 2 dpi.

I: Chimerism rates of monocytes in dura compared to chimerism of skull monocytes, or femur monocytes, in control or infected head shielded mice. n=6-8 from at least three independent experiments. Statistics by two-way ANOVA followed Šídák's multiple comparisons test, ****p<0.0001, ns = non significant.

J: Fluorescent intensity of GFP signal in divided by area in whole mounted dura as shown in representative images in S3I. N=3, *p<0.05, **p<0.01

K: Representative microscopy images of femur or skull bone marrow, or whole mount dura after bone marrow transfer from *Cx3cr1*$^{gfp/+}$ donor. The mice were either fully irradiated, or they were head shielded. A group of head shielded mice was infected. Scale bar = 50 µm.

L: Chimerism of DM post infection measured by flow cytometry. Statistics by unpaired t-test. n=6-8, from at least three independent experiments. *p< 0.05

M: Femur and skull bone marrow from infected *Ms4a3*^{Cre}*;R26*^{Tomato} mice labelled with GBS-AF633 (depicted in yellow). GBS is marked with white arrows. Scale bar =10 µm.

N: Numbers of CMP per femur or skull marrow in steady state and infection. Statistics by multiple unpaired t-test followed by the Holm-Šídák, n=5-7, data represents at least two independent experiments. ns = not significant.

O: Numbers of GMP of femur or skull marrow in steady state and infection. Statistics by multiple unpaired t-test followed by the Holm-Šídák, n=5-7, data represents at least two independent experiments. ***$p < 0.001$, ****$p < 0.0001$.

P: Numbers of MDPs of femur or skull marrow in steady state and infection. Statistics by multiple unpaired t-test followed by the Holm-Šídák, n=4-6, data represents at least two independent experiments. ns = not significant, ***$p < 0.001$.

Q: Numbers of monocyte progenitors (including cMOP and iMOP) of femur or skull marrow in steady state and infection. Statistics by multiple unpaired t-test followed by the Holm-Šídák, n=4-6, data represents three independent experiments. ns = not significant, ***$p < 0.001$.

R: Numbers of monocytes of femur or skull marrow in steady state and infection Statistics by multiple unpaired t-test followed by the Holm-Šídák, n=4-6, data represents at least two independent experiments. ns = not significant, *$p < 0.05$.

Fig. 4

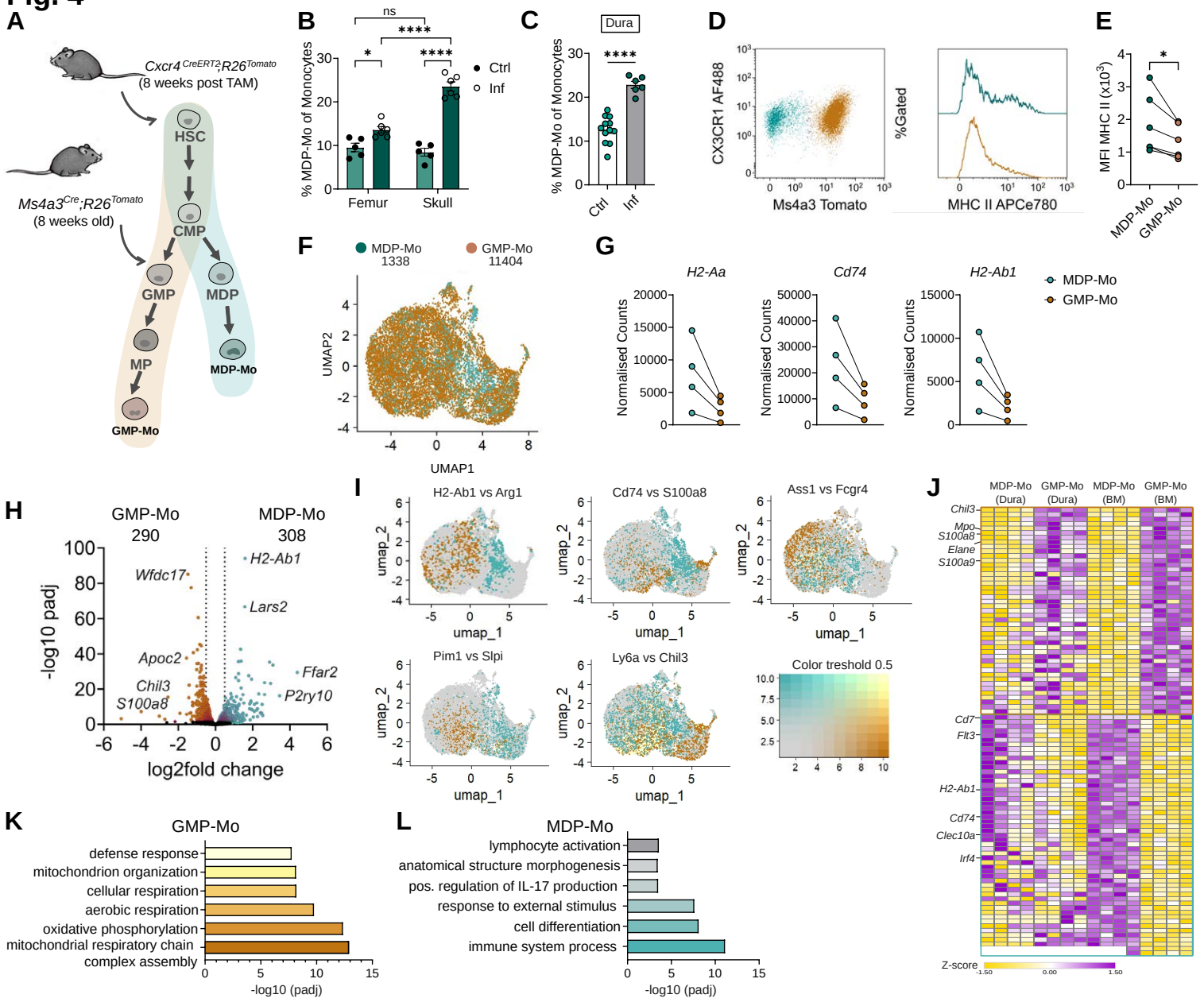
A
Cxcr4 CreERT2;R26Tomato
(8 weeks post TAM)
Ms4a3Cre;R26Tomato
(8 weeks old)
HSC
CMP
GMP
MDP
MP
MDP-Mo
GMP-Mo
B
ns
****
*
****
% MDP-Mo of Monocytes
Ctrl
Inf
Femur
Skull
C
Dura
****
% MDP-Mo of Monocytes
Ctrl
Inf
D
CX3CR1 AF488
Ms4a3 Tomato
%Gated
MHC II APCe780
E
*
MFI MHC II (x10³)
MDP-Mo
GMP-Mo
F
MDP-Mo 1338
GMP-Mo 11404
UMAP2
UMAP1
G
H2-Aa
Cd74
H2-Ab1
Normalised Counts
MDP-Mo
GMP-Mo
H
GMP-Mo 290
MDP-Mo 308
Wfdc17
H2-Ab1
Lars2
Apoc2
Chil3
S100a8
Ffar2
P2ry10
-log10 padj
log2fold change
I
H2-Ab1 vs Arg1
Cd74 vs S100a8
Ass1 vs Fcgr4
Pim1 vs Slpi
Ly6a vs Chil3
Color treshold 0.5
umap_1
umap_2
J
MDP-Mo (Dura)
GMP-Mo (Dura)
MDP-Mo (BM)
GMP-Mo (BM)
Chil3
Mpo
S100a8
Elane
S100a9
Cd7
Flt3
H2-Ab1
Cd74
Clec10a
Irf4
Z-score
K
GMP-Mo
defense response
mitochondrion organization
cellular respiration
aerobic respiration
oxidative phosphorylation
mitochondrial respiratory chain complex assembly
-log10 (padj)
L
MDP-Mo
lymphocyte activation
anatomical structure morphogenesis
pos. regulation of IL-17 production
response to external stimulus
cell differentiation
immune system process
-log10 (padj)

Fig. 4: GBS infection reprograms monocyte ontogeny toward MDP-derived lineages

A: Scheme of either GMP or MDP-derived monocyte lineages and respective mouse models used to either label GMP-derived cells (*Ms4a3*^{Cre};*R26*^{Tomato}) or all hematopoietic cells (*Cxcr4*^{CreERT2};*R26*^{Tomato}).

B: Percentage of MDP-Mo in skull and femur bone marrow from 8-week old *Ms4a3*^{Cre};*R26*^{Tomato} mice. n=5-6, from two independent experiments. Statistics by two-way ANOVA and Tukey's multiple comparisons test. ns=not significant, *p<0.05,****p<0.0001.

C: Percentage of MDP-Mo from dura of *Ms4a3*$^{Cre/+}$;*R26*$^{Tomato/+}$ mice. Statistics by unpaired t-test, n=6-12, from three independent experiments. ****p<0.0001.

D: Representative flow cytometry plots showing histograms of MHC-II expression in MDP-Mo (blue) and GMP-Mo (orange).

E: The difference in MHC-II expression in MDP-Mo and GMP-Mo, measured as MFI from figure D. Statistics by paired t-test, n=6, from two independent experiments.

F: UMAP representation based on gene expression profiling of sorted GMP-Mo and MDP-Mo from infected dura of *Ms4a3*^{Cre};*R26*^{Tomato} mice. The number of analyzed cells per condition is indicated.

G: Normalized counts of *H2-Aa*, *Cd74* and *H2-Ab1* in MDP-Mo and GMP-Mo, from pseudo-bulk analysis.

H: Volcano plot from pseudo-bulk analysis comparing DEG in MDP-Mo (right) and GMP-Mo (left). DEG are defined as padj<0.05 and $\log_2$(fold change)>0.5. The number of DEGs is indicated.

I: Feature maps showing selected genes differentially upregulated in GMP-Mo (orange) or MDP-Mo (blue), while cells expressing both are marked in yellow.

J: Heatmap comparing DEG from GSE262369 (MDP-Mo and GMP-Mo from steady state bone marrow) with pseudo-bulk analysis from infected dura MDP-Mo and GMP-Mo.

L-M: GO Terms for biological processes in GMP-Mo **(L)** or MDP-Mo **(M)**, with exclusions of the genes overlapping with GSE262369. Only some GO Terms are represented. The whole list can be found in Suppl. Table 1.

Fig. 5

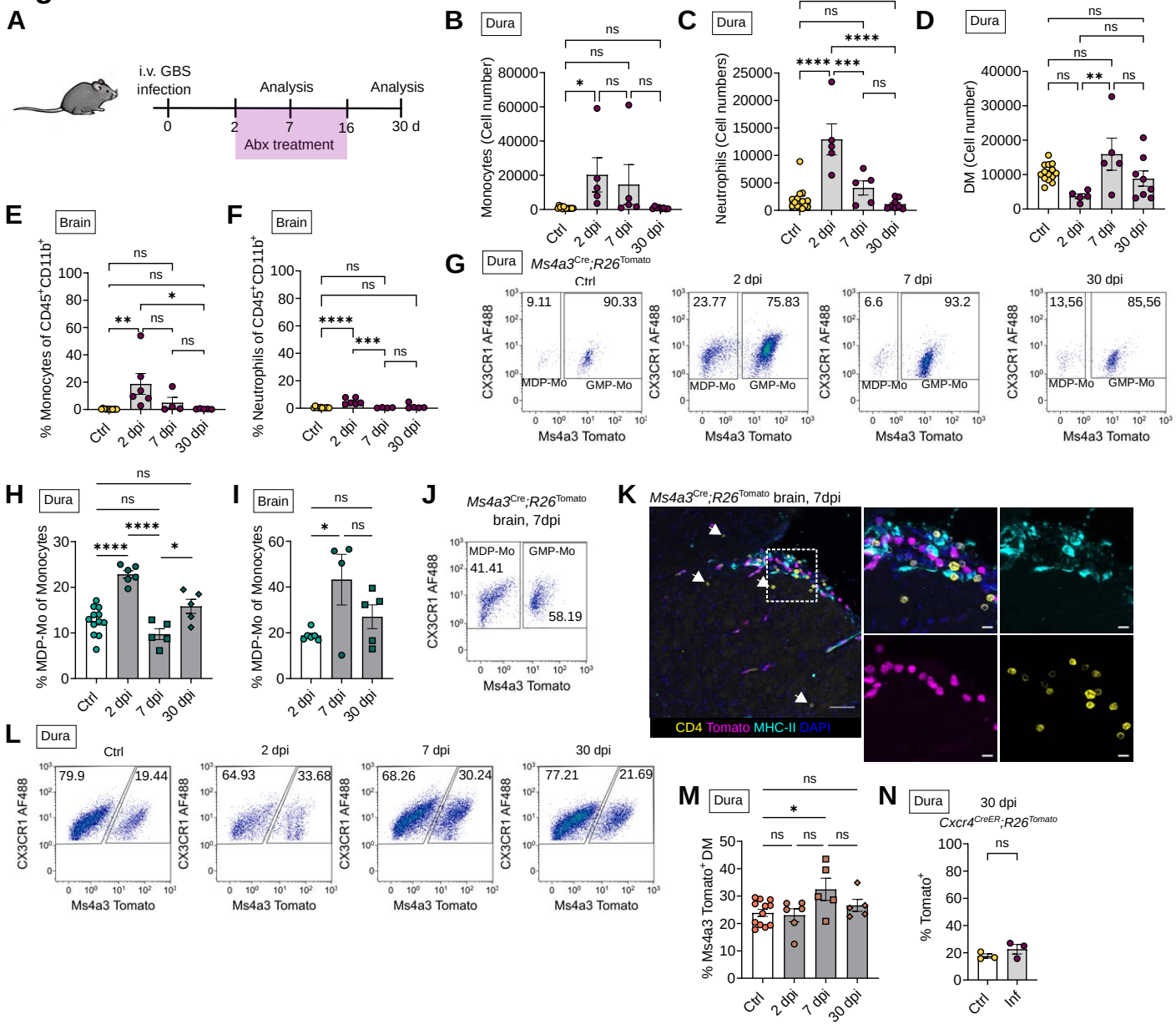
A
i.v. GBS infection
Analysis
Analysis
0
2
7
16
30 d
Abx treatment
B
Dura
Monocytes (Cell number)
Ctrl
2 dpi
7 dpi
30 dpi
C
Dura
Neutrophils (Cell numbers)
D
Dura
DM (Cell number)
E
Brain
% Monocytes of CD45+CD11b+
F
Brain
% Neutrophils of CD45+CD11b+
G
Dura
Ms4a3Cre;R26Tomato
Ctrl
2 dpi
7 dpi
30 dpi
CX3CR1 AF488
Ms4a3 Tomato
MDP-Mo
GMP-Mo
9.11
90.33
23.77
75.83
6.6
93.2
13,56
85,56
H
Dura
% MDP-Mo of Monocytes
I
Brain
% MDP-Mo of Monocytes
J
Ms4a3Cre;R26Tomato
brain, 7dpi
41.41
58.19
K
Ms4a3Cre;R26Tomato brain, 7dpi
CD4 Tomato MHC-II DAPI
L
Dura
79.9
19.44
64.93
33.68
68.26
30.24
77.21
21.69
M
Dura
% Ms4a3 Tomato+ DM
N
Dura
30 dpi
Cxcr4CreER;R26Tomato
% Tomato+
Inf

Fig. 5: Post-infection monocyte ontogeny diverges between dura and brain

A: Scheme of experimental setup for antibiotic treatment. Control mice were not infected, but were treated with antibiotics for the indicated time.

B-D: Monocyte (B), neutrophil (C) and DM (D) numbers in dura at 2, 7 and 30 dpi. Statistics by one-way ANOVA, followed by Tukey's multiple comparisons test. N=5-14, from at least three independent experiments.

E-F: Monocyte (E) and neutrophil (F) frequences in the brain at 2, 7 and 30 dpi. Statistics by one-way ANOVA, followed by Tukey's multiple comparisons test. n=4-12, from at least two independent experiments.

G: Flow cytometry plots representing changes in MDP-Mo and GMP-Mo frequencies in dura over time, from *Ms4a3*^{Cre};*R26*^{Tomato} mice. Percentages of MDP-Mo and GMP-Mo are written in the gates.

H: Percentages of MDP-Mo out of all monocytes in dura. Statistics by one-way ANOVA, followed by Tukey's multiple comparisons test. n=5-12, from at least three independent experiments.

I: Percentages of MDP-Mo out of all monocytes in brain. Statistics by one-way ANOVA, followed by Tukey's multiple comparisons test. n=4-6, from at least two independent experiments.

J: Representative flow cytometry plot showing MDP-Mo and GMP-Mo frequencies in brain at 7 dpi, from *Ms4a3*^{Cre};*R26*^{Tomato}mice. Percentages of MDP-Mo and GMP-Mo are written in the gates.

K: Representative microscopy image of sagittal brain section from *Ms4a3*^{Cre};*R26*^{Tomato}mice at 7 dpi. Dasher rectangle represents the magnified picture on the right. Arrows point to the parenchymal CD4 T-cells. Scale bar (left)= 50 µm. Scale bar (right)= 10 µm.

L: Flow cytometry plots representing changes in Tomato-positive and negative DM in dura over time, from *Ms4a3*^{Cre};*R26*^{Tomato} mice.

M: Percentages of Tomato-positive DM in dura over time, from *Ms4a3*^{Cre};*R26*^{Tomato} mice. Statistics by one-way ANOVA, followed by Tukey's multiple comparisons test. n=5-12, from at least two independent experiments.

N: Percentages of Tomato-positive DM in dura at 30 dpi, from *Cxcr4*^{CreERT2};*R26*^{Tomato} mice. Statistics by Student t-test, n=3.